Coupling Biot and Navier-Stokes problems for fluid-poroelastic structure interaction

Santiago Badia[a,1], Annalisa Quaini[b], Alfio Quarteroni[c,b]

[a] *International Center for Numerical Methods in Engineering (CIMNE), Universitat Politècnica de Catalunya, Jordi Girona 1-3, Edifici C1, 08034 Barcelona, Spain.*
[b] *Chair of Modelling and Scientific Computing (CMCS), Institute of Analysis and Scientific Computing (IACS), École Polytechnique Fédérale de Lausanne, CH-1015, Lausanne, Switzerland.*
[c] *MOX– Modellistica e Calcolo Scientifico Dipartimento di Matematica "F. Brioschi" Politecnico di Milano via Bonardi 9, 20133 Milano, Italy.*

Abstract

The interaction between a fluid and a poroelastic structure is a complex problem that couples the Navier-Stokes equations for the fluid with the Biot system for the structure. The finite element approximation of this problem is involved due to the fact that both subproblems are indefinite. In this work, we design residual-based stabilization techniques for the Biot system, that have been motivated using the variational multiscale approach. Then, we state the monolithic Navier-Stokes/Biot system with the appropriate transmission conditions on the interface. We consider both monolithic solvers and heterogeneous domain decomposition strategies. Different domain decomposition methods are used and their convergence has been analyzed for a simplified problem. The efficiency of these methods has been compared for a test problem motivated from hemodynamics applications.

Key words: Stabilized finite elements, Darcy's problem, Biot system, Poromechanics, Hemodynamics, Fluid-structure interaction
2000 MSC: 65M12, 65M60

1. Introduction

The arterial wall is made of three layers of tissue called intima, media, and adventitia. From the arterial lumen (where blood flows), the blood enters the intima and, after crossing the media, serves the adventitia and muscle cells. Hence, simulating the blood-artery interaction *neglecting the porosity of the artery wall means to disregard an important feature*. Modeling the poroelastic behaviour of the artery wall in an accurate and efficient way represents a step forward towards the numerical simulations of complex clinical problems. Let us mention two examples.

It is believed that accumulation of low density lipoproteins (LDL) leads to the initiation of atherosclerosis. The LDL concentration is affected by the filtration flow through the intima. In turn, the velocity of this flow is coupled to the deformation of the artery wall. Assuming that the LDL concentration has no effect on the motion of the artery

Email addresses: sbadia@cimne.upc.edu (Santiago Badia), annalisa.quaini@epfl.ch (Annalisa Quaini), alfio.quarteroni@epfl.ch (Alfio Quarteroni)

[1] The first author's research was supported by the the European Community through the Marie Curie contract *NanoSim* (MOIF-CT-2006-039522).

(or blood flow solution), a coupled fluid-porous structure problem must be considered to simulate this phenomenon.

Nano-sized delivery vehicles are emerging as powerful tools for treating and imaging cardiovascular disease (see, e.g., [38]). One method that has been proposed to treat vulnerable plaques and diffuse atherosclerosis in the large arteries involves injecting a drug compound into the bloodstream with a catheter to transport the drug to the surrounding tissue. The filtration velocity is the one that transports the drug inside the tissue. Again, the simulation of these phenomena requires a fluid-structure interaction (FSI) methodology where the artery wall is modeled as a porous medium.

The classical fluid-structure interaction problem that appears in hemodynamics (Navier-Stokes coupled to the elasticity for thin structures) has been broadly studied (see, e.g., [57, 20] and references therein). Many works have been devoted also to the Navier-Stokes/Darcy coupling (see, e.g., [54, 55, 4] and references therein) to simulate mass transport from the arterial lumen to the arterial walls and inside the walls, which are supposed to be rigid. The fluid-poroelastic structure interaction (FPSI) problem couples the Navier-Stokes equations for an incompressible fluid to the Biot problem, which govern the motion of a saturated poroelastic medium. This latest coupling has deserved much less attention. For hemodynamics applications, the most salient work is [46], where the Biot system is stated in terms of the structural velocity $\boldsymbol{u}_s$ (or displacement), filtration flux $\boldsymbol{q}$, and pressure p_p. The coupled system is linearized by Newton's method and solved by a monolithic solver. A simplified FPSI system appearing in hemodynamics has also been considered in [19]. Therein, the Biot system is written in terms of $(\boldsymbol{u}_s, p_p)$ only, after neglecting the inertia terms in Darcy's law. The fact that $\boldsymbol{q}$ does not appear in the formulation requires to introduce artificial boundary conditions on the interface.

Even though it is common practice to write the Darcy problem as a pressure Poisson equation, we did not adopt this approach here for many reasons. The original Darcy's law is a transient problem (see [29]), and inertia terms must be neglected in order to obtain the pressure Poisson problem. Much more critical is the fact that the Poisson problem fails to approximate non-smooth pressures in areas with jumps of physical parameters (e.g. hydraulic conductivity or porosity). The local pressure instabilities appearing in these areas are well-known in soil consolidation computations and motivated mixed formulations in [65]. However, the main reason why the Darcy's system has to be stated in mixed form is that we want to couple this problem with the Navier-Stokes equation via proper transmission conditions. The fact that $\boldsymbol{q}$ appears explicitly in the formulation is of great importance, because it allows to enforce the proper boundary conditions at the fluid-porous structure interface (see Section 4.1).

The discretization of the FPSI problem is challenging due to the three inf-sup conditions that make the coupled problem well-posed: the inf-sup condition for the fluid sub-problem and the inf-sup conditions for both incompressible elasticity and Darcy's problem for the poroelastic subproblem. While there exists a great variety of stabilization techniques for the incompressible Navier-Stokes equations, very few works deal with the stabilization of the Biot system in mixed form (no pressure Poisson equation is used). For instance, the Biot system in terms of $(\boldsymbol{u}_s, \boldsymbol{q}, p_p)$ has been approximated using a characteristic-based splitting algorithm in [65] and using penalty terms in [21] and references therein. In this work, we introduce a residual-based stabilization technique motivated by the variational multiscale method (VMS). This technique, introduced in [40], allows to use finite element spaces that do not satisfy the inf-sup conditions at the discrete level. The associated algebraic system is pretty involved, and the use of the same finite element spaces for all the velocities and pressures greatly simplifies the discretization and the enforcement of transmission conditions. We will consider linear Lagrangian elements for all the unknowns in the numerical experiments.

We extend to FPSI problems some of the strategies adopted for fluid-elastic structure interactions. Unlike [46, 19], we choose a fixed point method for the linearization of the Navier-Stokes/Biot coupled system. In this way, it is easy to consider the semi-implicit versions of all the algorithms, i.e. only one fixed point iteration is performed per time step. Semi-implicit methods enable us to better understand the Navier-Stokes/Biot coupling since nonlinearities are explicitly treated. To solve the linear FPSI system, we propose to extend both the monolithic approach introduced in [7] and partitioned procedures based on domain decomposition preconditioners. Up to our knowledge, it is the first time that a modular approach is adopted for FPSI problems. Among all the partitioned procedures, we focus our attention on the Dirichlet-Neumann, Robin-Neumann, and Robin-Robin algorithms (see, e.g., [60]).

The main objectives of this work are:

- the development of a residual-based stabilized finite element method for the Biot system;
- the statement of a monolithic Navier-Stokes/Biot system, the extension of domain decomposition techniques to this problem, which are compared with monolithic solvers.

In Section 2 we state the Navier-Stokes/Biot coupled problem in its differential form, specifying the coupling conditions which lead to a mathematically well-posed problem. The variational formulation of the coupled problem is tackled in Section 3. In Section 4 we develop a $(\boldsymbol{u}_s, \boldsymbol{q}, p_p)$ residual-based stabilized formulation of the Biot system. The matrix form of the Navier-Stokes/Biot system associated to the fully discretized and linearized problem is described in Section 5. Sections 6 and 7 present our monolithic approach and the partitioned procedures we apply to solve the linear system. Finally, in Section 8, we carry out some numerical experiments on simplified $2d$ problems representing blood-vessel systems.

2. Problem setting

Suppose that a bounded, polyhedral, and moving domain $\Omega_t \subset \mathbb{R}^d$ (d=2, 3, being the space dimension, and $t \in [0, T]$ the time) is made up of two regions, Ω_t^f and Ω_t^p, separated by a common interface $\Sigma_t = \partial\Omega_t^f \cap \partial\Omega_t^p$. The first region Ω_t^f is occupied by an incompressible and Newtonian fluid, and the second one Ω_t^p is occupied by a fully-saturated poroelastic matrix. Both domains depend on time. Here, we denote by $\boldsymbol{n}$ the unit normal vector on the boundary $\partial\Omega_t^f$, directed outwards into Ω_t^p, and by $\boldsymbol{t}$ the unit tangential vector orthogonal to $\boldsymbol{n}$. We assume the boundary $\partial\Omega_t$ (and so $\boldsymbol{n}$ and $\boldsymbol{t}$) to be regular enough.

The fluid problem is governed by the incompressible Navier-Stokes equations, whose Eulerian form reads:

$$\partial_t \boldsymbol{u}_f + \boldsymbol{u}_f \cdot \nabla \boldsymbol{u}_f - \frac{1}{\rho_f} \nabla \cdot \boldsymbol{\sigma}_f = \boldsymbol{f}_f \qquad \text{in } \Omega_t^f \times (0, T), \tag{1a}$$

$$\nabla \cdot \boldsymbol{u}_f = 0 \qquad \text{in } \Omega_t^f \times (0, T), \tag{1b}$$

where $\boldsymbol{u}_f$ is the fluid velocity, $\boldsymbol{\sigma}_f$ the Cauchy stress tensor and $\boldsymbol{f}_f$ the body force. The symbol ∇ denotes the spatial gradient operator and ∂_t denotes the spatial time derivative. For Newtonian fluids, $\boldsymbol{\sigma}_f$ has the following expression

$$\boldsymbol{\sigma}_f(\boldsymbol{u}_f, p_f) = -p_f \mathbf{I} + 2\mu\boldsymbol{\epsilon}(\boldsymbol{u}_f),$$

where p_f is the pressure, μ is the fluid viscosity, and

$$\boldsymbol{\epsilon}(\boldsymbol{u}_f) = \frac{1}{2}(\nabla \boldsymbol{u}_f + (\nabla \boldsymbol{u}_f)^T)$$

is the strain rate tensor.

In an elementary volume of the saturated porous structure we distinguish between the skeleton, composed by solid grains and void porous spaces, and the fluid phase, that consists of the fluid filling the pores. The porous medium is defined as the superposition of two continuous media, the skeleton and the fluid phase. Both fluid and solid are assumed to be incompressible, since the artery tissue is an incompressible material. The dynamics of such a medium are described by the Biot system [10, 11, 12], which in Eulerian description consists of:

$$\rho_p \mathrm{D}_t \boldsymbol{u}_s + \rho_d \mathrm{D}_t \boldsymbol{q} - \nabla \cdot \boldsymbol{\sigma}_s^{\mathrm{dev}}(\boldsymbol{\eta}) + \nabla p_p = \boldsymbol{f}_s \qquad \text{in } \Omega_t^p \times (0,T), \tag{2a}$$

$$\rho_d \mathrm{D}_t \boldsymbol{u}_s + \rho_d \mathrm{D}_t \frac{\boldsymbol{q}}{\phi} + \kappa^{-1}\boldsymbol{q} + \nabla p_p = \boldsymbol{f}_d \qquad \text{in } \Omega_t^p \times (0,T), \tag{2b}$$

$$\nabla \cdot (\boldsymbol{u}_s + \boldsymbol{q}) = 0 \qquad \text{in } \Omega_t^p \times (0,T). \tag{2c}$$

System (2) is made of the momentum equation for the balance of the total forces (2a), the momentum conservation equation for the fluid phase only (2b), and the incompressibility constraint (2c). In system (2), ρ_d is the density of the fluid in the pores, $\rho_p = \rho_s(1-\phi) + \rho_d\phi$ is the density of the saturated porous medium, where ρ_s is the density of the skeleton and ϕ the porosity. The porosity is the ratio of the pore volume over the total volume (pore + skeleton). We denote by $\boldsymbol{u}_s$ the velocity of the skeleton and by $\boldsymbol{q}$ the filtration velocity, i.e. the relative velocity of the fluid phase with respect to the solid one, $\boldsymbol{q} = \phi(\boldsymbol{u}_d - \boldsymbol{u}_s)$. Here, $\boldsymbol{u}_d$ is the velocity of the fluid in the porous medium. The hydraulic conductivity tensor is indicated with κ. $\boldsymbol{\sigma}_s^{\mathrm{dev}}$ is the deviatoric stress in the porous medium, supported by the solid phase only. The stress tensor $\boldsymbol{\sigma}_s^{\mathrm{dev}}$ is related to the displacement of the porous structure $\boldsymbol{\eta}$ (usually, in the reference configuration) by a suitable constitutive law. E.g., for an incompressible elastic solid, it reads

$$\boldsymbol{\sigma}_s^{\mathrm{dev}}(\boldsymbol{\eta}) = 2\mu_\ell \mathrm{dev}\left[\boldsymbol{\epsilon}(\boldsymbol{\eta})\right],$$

where μ_ℓ is the Lamé constant of the porous matrix. The volumetric stress in the porous medium is $-p_p\mathbf{I}$, where p_p is the pressure in the porous medium. Thus, the total Cauchy stress for the porous medium is $\boldsymbol{\sigma}_p = -p_p\mathbf{I} + \boldsymbol{\sigma}_s^{\mathrm{dev}}$. We refer to [29] for a detailed discussion about the macroscopic split of stresses into solid and fluid phase contributions. Finally, D_t denotes the classical concept of material derivative. The right-hand side vectors $\boldsymbol{f}_s$ and $\boldsymbol{f}_d$ account for external body forces. In the subsequent discussion, the values of densities, porosity, and hydraulic conductivity are assumed to be constant in space and time.

The Biot system (2) is widely employed to model geotechnical problems. In this kind of applications $\mathrm{D}_t\boldsymbol{q}$ is usually neglected in order to end up with a pressure Poisson equation. As commented above, this approach is not acceptable when coupling Biot and Navier-Stokes systems. Thus, we will consider the mixed formulation (2) without further approximations.

In the following, the boundary conditions on $\partial\Omega_t \backslash \Sigma_t$ are chosen in a classical simple form, since they play no essential role in the interaction. On the exterior boundary of the porous medium we shall impose *drained* conditions ($p_p = 0$) on the pressure and *clamped* conditions ($\boldsymbol{u}_s = \mathbf{0}$) on the structure velocity at the inlet and outlet. In Fig. 1, we specify the boundary conditions imposed on $\partial\Omega_t$ for the $2d$ simulation of the Navier-Stokes/Biot system in Section 8.

The objective of the next subsection is to identify a physically consistent set of interface conditions which couple the Biot system to the incompressible Navier-Stokes equations. The variational statement of the resulting problem must lead to a mathematically well-posed initial-boundary-value problem.

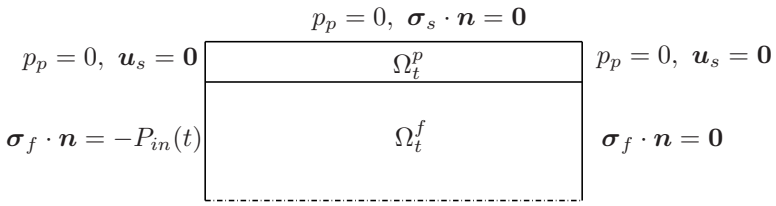

Figure 1: Boundary conditions imposed on the physical boundary of the $2d$ problem in Section 8.

2.1. The coupling conditions and the Biot/Navier-Stokes system

The natural transmission conditions at the interface of a fluid and an impervious elastic solid consist of continuity of velocities and stresses. In order to understand the coupling between a fluid and a deformable and porous medium, we first review the transmission relations for a fluid in contact with a rigid but porous solid matrix in a steady-state case. We have two distinct scales of hydrodynamics: the first one is represented by the Navier-Stokes system and the second one by the Darcy equations

$$\kappa^{-1}\boldsymbol{q} + \nabla p_p = \boldsymbol{f}_d \qquad \text{in } \Omega^p, \tag{3a}$$

$$\nabla \cdot \boldsymbol{q} = 0 \qquad \text{in } \Omega^p. \tag{3b}$$

Fluid mass conservation is a natural requirement at the interface, and continuity of pressure or vanishing tangential velocity of the viscous fluid are other classically assumed conditions [34, 48]. However, these issues have been controversial, see [66]. In fact, the location of the interface itself is uncertain, since the porous medium is a mixture of fluid and solid. Furthermore, Beavers and Joseph [9] discovered that a fluid in contact with a porous medium flows faster along the interface than a fluid in contact with a solid surface. This means that there is a slip of the fluid at the interface with a porous medium. To represent it, they proposed that the normal derivative of the tangential component of the fluid velocity $\boldsymbol{u}_f \cdot \boldsymbol{t}$ would satisfy

$$\frac{\partial(\boldsymbol{u}_f \cdot \boldsymbol{t})}{\partial n} = \frac{\gamma}{\sqrt{\kappa}}(\boldsymbol{u}_f \cdot \boldsymbol{t} - \boldsymbol{q} \cdot \boldsymbol{t}),$$

where γ is the slip rate coefficient. This condition was developed further in [63, 45]. A rigorous analysis of such interface conditions can be found in [43, 44]. See [56, 51] for insights on those interface conditions and [64, 39, 47, 32, 4] for numerical works.

Any model of fluid in contact with a deformable and porous medium contains the filtration velocity, in addition to the displacement (or velocity) and stress variations of the porous matrix.

For a discussion on the coupling between a Stokes flow and a poroelastic medium, see [54, 55, 67]. Following [67], we begin with the mass conservation requirement that the normal fluid flux must be continuous across the interface. Thus, the solution of the coupled problem (1)-(2) is required to satisfy the *admissibility* constraint

$$\boldsymbol{u}_f \cdot \boldsymbol{n} = (\boldsymbol{u}_s + \boldsymbol{q}) \cdot \boldsymbol{n}. \tag{4a}$$

For the balance of the normal stresses in the fluid phase across Σ_t, we have

$$\boldsymbol{n} \cdot (\boldsymbol{\sigma}_f \cdot \boldsymbol{n}) = -p_p. \tag{4b}$$

The conservation of momentum requires that the total stress of the porous medium is balanced by the total stress of the fluid:

$$\boldsymbol{\sigma}_p \cdot \boldsymbol{n} = \boldsymbol{\sigma}_f \cdot \boldsymbol{n}. \tag{4c}$$

Finally, the fluid tangential stress (which is equal to the one of the solid phase) is assumed to be proportional to the slip rate according to the Beavers-Joseph-Saffman condition

$$\boldsymbol{t} \cdot (\boldsymbol{\sigma}_f \cdot \boldsymbol{n}) = -\frac{\gamma}{\sqrt{\kappa}} (\boldsymbol{u}_f - \boldsymbol{u}_s) \cdot \boldsymbol{t}. \tag{4d}$$

We shall show next that interface conditions (4) suffice to precisely couple the Biot system (2) in Ω_t^p to the Navier-Stokes one (1) in Ω_t^f.

3. Weak formulation

The purpose of this section is to construct an appropriate variational formulation of the Navier-Stokes/Biot system (1)-(2) coupled by interface conditions (4). Let us introduce some standard notation. The space of functions whose p power ($1 \leq p < \infty$) is integrable in a domain Ω is denoted by $L^p(\Omega)$, $L^\infty(\Omega)$ being the space of bounded functions in Ω (in the Lebesgue sense). The space of functions whose distributional derivatives of order up to $m \geq 0$ (integer) belong to $L^2(\Omega)$ is denoted by $H^m(\Omega)$. The space $H_0^1(\Omega)$ consists of functions in $H^1(\Omega)$ vanishing on $\partial\Omega$. The topological dual of $H_0^1(\Omega)$ is denoted by $H^{-1}(\Omega)$. The space of vector-valued functions with components in $L^2(\Omega)$ is denoted with $L^2(\Omega)^d$, and analogously for the rest of scalar spaces. $H(\mathrm{div}, \Omega)$ is the space of functions in $L^2(\Omega)^d$ with their divergence in $L^2(\Omega)$. $H_0(\mathrm{div}, \Omega)$ is the space of vector fields in $H(\mathrm{div}, \Omega)$ with zero normal trace on $\partial\Omega$. We also recall that the space of traces of $H^1(\Omega)$ on a line (surface for three dimensions) $\beta \subset \Omega$ is denoted by $H^{1/2}(\beta)$. The topological dual of $H^{1/2}(\beta)$ is the space of fluxes denoted by $H^{-1/2}(\beta)$.

We define two families of mappings that will track the domain in time:

$$\begin{aligned} \mathcal{L} &: \Omega_0^p \times [0,T] \longrightarrow \Omega_t^p, \ (\boldsymbol{x}_0, t) \longrightarrow \boldsymbol{x} = \mathcal{L}(\boldsymbol{x}_0, t), \\ \mathcal{A} &: \Omega_0^f \times [0,T] \longrightarrow \Omega_t^f, \ (\boldsymbol{x}_0, t) \longrightarrow \boldsymbol{x} = \mathcal{A}(\boldsymbol{x}_0, t). \end{aligned}$$

The map $\mathcal{L}_t = \mathcal{L}(\cdot, t)$ tracks the solid domain in time, $\mathcal{A}_t = \mathcal{A}(\cdot, t)$ the fluid domain and they must agree on Σ_t in order to define an homeomorphism over Ω_t. For the structure, we can adopt the material mapping

$$\mathcal{L}_t(\boldsymbol{x}_0) = \boldsymbol{x}_0 + \boldsymbol{\eta}(\boldsymbol{x}_0, t). \tag{5}$$

Apart from the matching condition on the interface, the fluid domain mapping $\mathcal{A}_t$ is arbitrary. This mapping can be defined as an appropriate extension operator $\mathrm{Ext}(\cdot)$ applied to its value on the interface:

$$\mathcal{A}_t(\boldsymbol{x}_0) = \boldsymbol{x}_0 + \mathrm{Ext}(\boldsymbol{\eta}(\boldsymbol{x}_0, t)|_{\Sigma_0}).$$

A classical choice is to consider a harmonic extension in the reference domain. $\mathcal{A}_t$ is called the *Arbitrary Lagrangian-Eulerian* (ALE) mapping, since in general it does not track the fluid particles (in that case the formulation would be purely Lagrangian).

Let us start with the weak form of the Navier-Stokes problem. We define the functional spaces

$$V^f(t) = \Big\{ \boldsymbol{v} : \Omega_t^f \to \mathbb{R}^d,\ \boldsymbol{v} = \hat{\boldsymbol{v}} \circ (\mathcal{A}_t)^{-1},\ \hat{\boldsymbol{v}} \in H^1(\Omega_0^f)^d \Big\},$$
$$Q^f(t) = \Big\{ q : \Omega_t^f \to \mathbb{R},\ q = \hat{q} \circ (\mathcal{A}_t)^{-1},\ \hat{q} \in L^2(\Omega_0^f) \Big\}. \tag{6}$$

$\mathcal{A}_t$ is assumed to be regular enough to satisfy $V^f(t) \subset H^1(\Omega_t^f)^d$. At any time value t, the weak form of the Navier-Stokes problem consists of finding $(\boldsymbol{u}_f, p_f) \in V^f(t) \times Q^f(t)$ such that

$$\rho_f(\partial_t \boldsymbol{u}_f, \boldsymbol{v}^f)_{\Omega_t^f} + 2\mu_f \left(\boldsymbol{\epsilon}(\boldsymbol{u}_f), \boldsymbol{\epsilon}\left(\boldsymbol{v}^f\right)\right)_{\Omega_t^f} + \rho_f \int_{\Omega_t^f} (\boldsymbol{u}_f \cdot \nabla \boldsymbol{u}_f) \cdot \boldsymbol{v}^f \, \mathrm{d}\Omega$$
$$- \left(p_f, \nabla \cdot \boldsymbol{v}^f\right)_{\Omega_t^f} + (\nabla \cdot \boldsymbol{u}_f, q_f)_{\Omega_t^f} = \langle \boldsymbol{f}_f, \boldsymbol{v}^f \rangle_{\Omega_t^f} + \langle \boldsymbol{\sigma}_f \cdot \boldsymbol{n}, \boldsymbol{v}^f \rangle_{\Sigma_t} \tag{7}$$

for any $(\boldsymbol{v}_f, q_f) \in V^f(t) \times Q^f(t)$ This weak equation for every time value must be understood in a Lebesgue sense (in time), since the terms in (1) do not have to be $\mathcal{C}^0$ in time. This comment applies to the rest of weak formulations in space evaluated at a time value. The last term in equation (7) involves the fluid stresses over the interface.

In order to write the Biot system in its weak form, we introduce the functional spaces

$$V^s(t) = \Big\{ \boldsymbol{v} : \Omega_t^p \to \mathbb{R}^d,\ \boldsymbol{v} = \hat{\boldsymbol{v}} \circ (\mathcal{L}_t)^{-1},\ \hat{\boldsymbol{v}} \in H^1(\Omega_0^p)^d \Big\},$$
$$R(t) = \big\{ \boldsymbol{v} : \Omega_t^p \to \mathbb{R}^d,\ \boldsymbol{v} = \hat{\boldsymbol{v}} \circ (\mathcal{L}_t)^{-1},\ \hat{\boldsymbol{v}} \in H(\mathrm{div}, \Omega_0^p)^d \big\},$$
$$Q^p(t) = \big\{ q : \Omega_t^p \to \mathbb{R},\ q = \hat{q} \circ (\mathcal{L}_t)^{-1},\ \hat{q} \in L^2(\Omega_0^p) \big\}. \tag{8}$$

where $\mathcal{L}_t$ is assumed to be regular enough to satisfy $V^s(t) \subset H^1(\Omega_t^p)^d$. The weak form of the Biot system for a time value t consists of finding $(\boldsymbol{u}_s, \boldsymbol{q}, p_p) \in V^s(t) \times R(t) \times Q^p(t)$ such that

$$\rho_p(\mathrm{D}_t \boldsymbol{u}_s, \boldsymbol{v}^s)_{\Omega_t^p} + \rho_d(\mathrm{D}_t \boldsymbol{q}, \boldsymbol{v}^s)_{\Omega_t^p} + (\boldsymbol{\sigma}_s^{\mathrm{dev}}(\boldsymbol{\eta}), \nabla \boldsymbol{v}^s)_{\Omega_t^p} - (p_p, \nabla \cdot \boldsymbol{v}^s)_{\Omega_t^p}$$
$$+ \rho_d(\mathrm{D}_t \boldsymbol{u}_s, \boldsymbol{r})_{\Omega_t^p} + \frac{\rho_d}{\phi}(\mathrm{D}_t \boldsymbol{q}, \boldsymbol{r})_{\Omega_t^p} + \kappa^{-1}(\boldsymbol{q}, \boldsymbol{r})_{\Omega_t^p} - (p_p, \nabla \cdot \boldsymbol{r})_{\Omega_t^p}$$
$$+ (\nabla \cdot (\boldsymbol{u}_s + \boldsymbol{q}), q_p)_{\Omega_t^p} = \langle \boldsymbol{f}_s, \boldsymbol{v}^s \rangle_{\Omega_t^p} + \langle \boldsymbol{f}_d, \boldsymbol{r} \rangle_{\Omega_t^p} - \langle \boldsymbol{\sigma}_p \cdot \boldsymbol{n}, \boldsymbol{v}^s \rangle_{\Sigma_t} + (p_p, \boldsymbol{r} \cdot \boldsymbol{n})_{\Sigma_t} \tag{9}$$

for any $(\boldsymbol{v}^s, \boldsymbol{r}, q_p) \in V^s(t) \times R(t) \times Q^p(t)$. The last two terms in (9) involve the stress of the porous medium on the interface. None of the coupling conditions (4) has been imposed yet.

At this point, we can couple (1) and (9) by invoking the transmission conditions. Let us start with interface condition (4c). For any interface function $\boldsymbol{\xi} \in H^{1/2}(\Sigma_t)$, we have

$$\langle \boldsymbol{\sigma}_f \cdot \boldsymbol{n} - \boldsymbol{\sigma}_p \cdot \boldsymbol{n}, \boldsymbol{\xi} \rangle_{\Sigma_t} = 0.$$

Let us denote by $\mathcal{E}_t^f(\boldsymbol{\xi})$ and $\mathcal{E}_t^p(\boldsymbol{\xi})$ arbitrary extensions of $\boldsymbol{\xi}$ over Ω_t^f and Ω_t^p respectively. We can write the continuity of stresses (4c) in terms of the problem unknowns testing expressions (7) and (9) against $\mathcal{E}_t^f(\boldsymbol{\xi})$ and $\mathcal{E}_t^p(\boldsymbol{\xi})$, respectively. This approach leads to the weak continuity of stresses in the form of (10c) below (see, e. g., [8]).

We can express the boundary conditions (4b) and (4d) in the following way:

$$\langle \boldsymbol{\sigma}_f \cdot \boldsymbol{n} + p_p \boldsymbol{n} + \frac{\gamma}{\sqrt{\kappa}}((\boldsymbol{u}_f - \boldsymbol{u}_s) \cdot \boldsymbol{t})\boldsymbol{t}, \boldsymbol{\xi} \rangle_{\Sigma_t} = 0.$$

for any interface function $\boldsymbol{\xi} \in H^{1/2}(\Sigma_t)$. Again, this expression can be written in terms of the problem unknowns by testing expressions (7) and (9) against $\mathcal{E}_t^f(\boldsymbol{\xi})$ and $\mathcal{E}_t^p(\boldsymbol{\xi})$, respectively, leading to (10d) below.

In order to write the weak form of the coupled problem, let us denote by $V_0^f(t)$ and $V_0^s(t)$ the subspace of functions belonging to $V^f(t)$ and $V^s(t)$ respectively with null trace on Σ_t. Moreover, space $R_0(t)$ is spanned by all the functions in $R(t)$ with zero normal trace. The variational formulation reads:

Given $t \in (0,T)$, find $(\boldsymbol{u}_f, \boldsymbol{u}_s, \boldsymbol{q}, p_f, p_p)$ belonging to the corresponding functional spaces introduced above, satisfying the following system of equations

1. Fluid subproblem:

$$\rho_f(\partial_t \boldsymbol{u}_f, \boldsymbol{v}^f)_{\Omega_t^f} + 2\mu_f \left(\boldsymbol{\epsilon}\left(\boldsymbol{u}_f\right), \boldsymbol{\epsilon}\left(\boldsymbol{v}^f\right)\right)_{\Omega_t^f} + \rho_f \int_{\Omega_t^f} \left(\boldsymbol{u}_f \cdot \nabla \boldsymbol{u}_f\right) \cdot \boldsymbol{v}^f \, \mathrm{d}\Omega$$
$$- \left(p_f, \nabla \cdot \boldsymbol{v}^f\right)_{\Omega_t^f} + \left(\nabla \cdot \boldsymbol{u}_f, q_f\right)_{\Omega_t^f} = \langle \boldsymbol{f}_f, \boldsymbol{v}^f \rangle_{\Omega_t^f}. \tag{10a}$$

   for any $(\boldsymbol{v}^f, q_f) \in V_0^f(t) \times Q^f(t)$.
2. Biot subproblem:

$$\rho_p(\mathrm{D}_t \boldsymbol{u}_s, \boldsymbol{v}^s)_{\Omega_t^p} + \rho_d(\mathrm{D}_t \boldsymbol{q}, \boldsymbol{v}^s)_{\Omega_t^p} + (\boldsymbol{\sigma}_s^{\mathrm{dev}}(\boldsymbol{\eta}), \nabla \boldsymbol{v}^s)_{\Omega_t^p} - (p_p, \nabla \cdot \boldsymbol{v}^s)_{\Omega_t^p}$$
$$+ \rho_d(\mathrm{D}_t \boldsymbol{u}_s, \boldsymbol{r})_{\Omega_t^p} + \frac{\rho_d}{\phi}(\mathrm{D}_t \boldsymbol{q}, \boldsymbol{r})_{\Omega_t^p} + \kappa^{-1}(\boldsymbol{q}, \boldsymbol{r})_{\Omega_t^p} - (p_p, \nabla \cdot \boldsymbol{r})_{\Omega_t^p}$$
$$+ (\nabla \cdot (\boldsymbol{u}_s + \boldsymbol{q}), q_p)_{\Omega_t^p} = \langle \boldsymbol{f}_s, \boldsymbol{v}^s \rangle_{\Omega_t^p} + \langle \boldsymbol{f}_d, \boldsymbol{r} \rangle_{\Omega_t^p} \tag{10b}$$

   for any $(\boldsymbol{v}^s, \boldsymbol{r}, q_p) \in V_0^s(t) \times R_0(t) \times Q^p(t)$.
3. Continuity of total stresses:

$$\rho_f(\partial_t \boldsymbol{u}_f, \mathcal{E}_t^f(\boldsymbol{\xi}))_{\Omega_t^f} + 2\mu_f \left(\boldsymbol{\epsilon}\left(\boldsymbol{u}_f\right), \boldsymbol{\epsilon}\left(\mathcal{E}_t^f(\boldsymbol{\xi})\right)\right)_{\Omega_t^f} + \rho_f \int_{\Omega_t^f} \left(\boldsymbol{u}_f \cdot \nabla \boldsymbol{u}_f\right) \cdot \mathcal{E}_t^f(\boldsymbol{\xi}) \, \mathrm{d}\Omega$$
$$- \left(p_f, \nabla \cdot \mathcal{E}_t^f(\boldsymbol{\xi})\right)_{\Omega_t^f} + \rho_p(\mathrm{D}_t \boldsymbol{u}_s, \mathcal{E}_t^p(\boldsymbol{\xi}))_{\Omega_t^p} + \rho_d(\mathrm{D}_t \boldsymbol{q}, \mathcal{E}_t^p(\boldsymbol{\xi}))_{\Omega_t^p} + (\boldsymbol{\sigma}_s^{\mathrm{dev}}(\boldsymbol{\eta}), \nabla \mathcal{E}_t^p(\boldsymbol{\xi}))_{\Omega_t^p}$$
$$- (p_p, \nabla \cdot \mathcal{E}_t^p(\boldsymbol{\xi}))_{\Omega_t^p} = \langle \boldsymbol{f}_f, \mathcal{E}_t^f(\boldsymbol{\xi}) \rangle_{\Omega_t^f} + \langle \boldsymbol{f}_s, \mathcal{E}_t^p(\boldsymbol{\xi}) \rangle_{\Omega_t^p} \tag{10c}$$

   for any $\boldsymbol{\xi} \in H^{1/2}(\Sigma_t)$.
4. Continuity of normal stresses and Beaver-Joshep-Saffman condition:

$$\rho_f(\partial_t \boldsymbol{u}_f, \mathcal{E}_t^f(\boldsymbol{\zeta}))_{\Omega_t^f} + 2\mu_f \left(\boldsymbol{\epsilon}\left(\boldsymbol{u}_f\right), \boldsymbol{\epsilon}\left(\mathcal{E}_t^f(\boldsymbol{\zeta})\right)\right)_{\Omega_t^f} + \rho_f \int_{\Omega_t^f} \left(\boldsymbol{u}_f \cdot \nabla \boldsymbol{u}_f\right) \cdot \mathcal{E}_t^f(\boldsymbol{\zeta}) \, \mathrm{d}\Omega$$
$$- \left(p_f, \nabla \cdot \mathcal{E}_t^f(\boldsymbol{\zeta})\right)_{\Omega_t^f} + \rho_d(\mathrm{D}_t \boldsymbol{u}_s, \mathcal{E}_t^p(\boldsymbol{\zeta}))_{\Omega_t^p} + \frac{\rho_d}{\phi}(\mathrm{D}_t \boldsymbol{q}, \mathcal{E}_t^p(\boldsymbol{\zeta}))_{\Omega_t^p} + \kappa^{-1}(\boldsymbol{q}, \mathcal{E}_t^p(\boldsymbol{\zeta}))_{\Omega_t^p}$$
$$- (p_p, \nabla \cdot \mathcal{E}_t^p(\boldsymbol{\zeta}))_{\Omega_t^p} + \frac{\gamma}{\sqrt{\kappa}}(((\boldsymbol{u}_f - \boldsymbol{u}_s) \cdot \boldsymbol{t})\boldsymbol{t}, \boldsymbol{\zeta})_{\Sigma_t} = \langle \boldsymbol{f}_f, \mathcal{E}_t^f(\boldsymbol{\zeta}) \rangle_{\Omega_t^f} + \langle \boldsymbol{f}_d, \mathcal{E}_t^p(\boldsymbol{\zeta}) \rangle_{\Omega_t^p}. \tag{10d}$$

   for any $\boldsymbol{\zeta} \in H^{1/2}(\Sigma_t)$.
5. Continuity of fluxes (4a).

In this coupled problem, the continuity of stresses (4b)-(4d) have been weakly enforced. We refer to [68] for the use of variational transmission of interface loads for the FSI problem. It has been proved in [18] that a weak transmission of stresses is much superior to a strong one in terms of accuracy. Moreover, it is basic for stability reasons (see [68]).

4. Space and time discretization

In this section, we focus on the space and time discretization of the poroelastic subproblem (2). Let us start with the time discretization. We consider a backward-differencing scheme of order 1 (BDF1) (also called Backward Euler) for simplicity. For

a given time step t^{n+1} we define the BDF1 operator δ_t applied to a function $g(\boldsymbol{x},t)$ as $\delta_t g^{n+1}(\boldsymbol{x}) = \delta t^{-1}(g(t^{n+1},\boldsymbol{x}) - g(t^n,\boldsymbol{x}))$ where δt is the time step size. In any case, the following exposition can be extended to other time integrators.

The Eulerian time derivative in the fluid subproblem (10a) is not suitable for the time discretization of problems in moving domains. The reason is intuitive: at time step t^{n+1} we can find points belonging to $\Omega_{t^{n+1}}$ that did not belong to Ω_{t^n}. At these points, the discrete Eulerian time derivative of a function $g(\boldsymbol{x},t)$ defined over Ω_t, e.g. $\delta_t g^{n+1}(\boldsymbol{x})$, is meaningless, since $\boldsymbol{x} \notin \Omega_{t^n}$ and $g(t^n,\boldsymbol{x})$ is not defined. In order to solve this problem, we introduce the ALE derivative

$$\partial_t \boldsymbol{u}|_{\boldsymbol{x}_0} = \partial_t \boldsymbol{u} + \boldsymbol{w} \cdot \nabla \boldsymbol{u}, \tag{11}$$

which is the acceleration observed by a particle that moves with the fluid mapping $\mathcal{A}_t$. The domain velocity $\boldsymbol{w}$ is calculated using the following expression:

$$\boldsymbol{w}(\boldsymbol{x},t) = \partial_t \boldsymbol{x}|_{\boldsymbol{x}_0} = (\partial_t \mathcal{A}_t) \circ \mathcal{A}_t^{-1}(\boldsymbol{x}).$$

Then, the ALE form of the Navier-Stokes subproblem is obtained by invoking (11) in (10a). The discrete ALE derivative is denoted by $\delta_t g^{n+1}|_{\boldsymbol{x}_0}$. We denote by $\mathrm{d}_t g^{n+1}$ the discrete material derivative that is simply the time derivative of the structural nodal values, for a mesh that is moving with the Lagrangian mapping (5). Let us remark that the material time derivative is suitable for time discretization.

For the spatial discretization, let us denote by $\mathcal{T}_h = \{K\}$ the finite element (FE) partition composed by a set of finite elements, indicated by K. We will use the broken inner product $(\cdot,\cdot)_K = \sum_K (\cdot,\cdot)$, where $\sum_K$ denotes the summation over all the finite elements. Let $V_h^f(0)$, $Q_h^f(0)$, $V_h^s(0)$, $R_h(0)$, and $Q_h^p(0)$ be conforming FE spaces approximations of $V^f(0)$, $Q^f(0)$, $V^s(0)$, $R(0)$, and $Q^p(0)$, respectively. We extend those spaces in time as it has been done at the continuous level in (6)-(8), using mappings $\mathcal{A}_t$ and $\mathcal{L}_t$. From now on, we omit the time label from the FE spaces names.

The crude Galerkin approximation of the poroelastic problem (2) may fail because pressure stability can only be obtained for suitable FE pairs that satisfy appropriate inf-sup conditions (see [17]). The Darcy and the incompressible elasticity problems involve different inf-sup conditions. Inf-sup stable elements have been developed for the Darcy problem and for incompressible elasticity but, as far as we know, there are not inf-sup stable elements that are stable in both cases. An alternative to inf-sup stable elements is to resort to stabilized methods. The idea is to strengthen the classical variational formulation so that FE approximations, which would otherwise be unstable, become stable and convergent. We want to obtain a stabilized version of the Biot system that remains stable for both limits of the problem: the Darcy problem (as the rigidity of the structure goes to infinity) and the impervious structural problem (as the conductivity goes to zero). When the solid phase in the poroelastic medium is compressible, no stabilization is needed in the limit of an impervious structure. Anyway, when dealing with incompressible materials, as human tissues, stabilization is needed in this limit too.

Stabilization techniques for the Navier-Stokes problem can be found in many papers (see, e.g., [27, 23]) but there is much less work for the stabilization of the Biot problem in mixed form. The work of Salomoni and Schrefler [65] is one effort in this direction: the authors have used the non-consistent characteristic-based splitting (CBS) algorithm to analyze creep phenomena in consolidation processes.

In view of that, we consider first the (transient) Darcy problem. In subsection 4.1, we propose a stabilization that is an extension (in time) of the method in [49]. Then, we consider a stabilized technique for the incompressible elasticity problem in subsection 4.2. Finally, an original stabilization of the Biot system is suggested in subsection 4.3.

4.1. Stabilization of the Darcy problem

The (transient) Darcy problem can be regarded as a limit of the Biot system when the rigidity of the solid phase goes to infinity, i.e. the poroelastic structure is a rigid body. As commented above, there are two different approaches to solve equations (3): one involves a primal, single-field formulation for the pressure, while the other employs a mixed two-field formulation in which the variables are both velocity and pressure. However, when this problem is coupled to the Navier-Stokes system, the continuity of normal stress on the interface (4b) becomes a Dirichlet boundary condition over the Darcy pressure with data in $H^{-1/2}(\Sigma_t)$. Thus, this problem is ill-posed and *a mixed formulation is the only choice*.

The classical mixed variational formulation for flow in porous media is well-posed in the functional spaces $L^2(\Omega^p)$ and $(H(\mathrm{div},\Omega^p))^d$ for the pressure and velocity, respectively (see [17]). Finite element approximations of those spaces, which satisfy the inf-sup condition, can be found in [61, 69, 16, 15, 14]. As an alternative to inf-sup elements, we develop a stabilized variational formulation stemming from [49].

Let us consider the Darcy problem over a fixed domain Ω^p supplemented with homogeneous boundary conditions for the sake of clarity. The variational formulation of this problems at every time step (in weak sense in time) consists of finding $\boldsymbol{q} \in H_0(\mathrm{div},\Omega^p)$ and $p_p \in L^2(\Omega^p)$ such that:

$$\left(\frac{\rho_d}{\phi}\mathrm{D}_t\boldsymbol{q} + \kappa^{-1}\boldsymbol{q}, \boldsymbol{r}\right)_{\Omega^p} - (p_p, \nabla\cdot\boldsymbol{r})_{\Omega^p} = (\boldsymbol{f}_d, \boldsymbol{r})_{\Omega^p}, \tag{12a}$$

$$(\nabla\cdot\boldsymbol{q}, q_p)_{\Omega^p} = (g, q_p)_{\Omega^p}\,, \tag{12b}$$

for all $(\boldsymbol{r}, q_p) \in H_0(\mathrm{div},\Omega^p)\times L^2(\Omega)$, where g is the volumetric flow rate source or sink. The incompressible case is recovered simply by setting $g = 0$. The following results can easily be extended to either Neumann ($p_p = p_N$, with p_N a given function) or non-homogeneous Dirichlet ($\boldsymbol{q}\cdot\boldsymbol{n} = q_D$, q_D known) boundary conditions as well as moving domains. At the continuous level, the well-possedness of this problem is due to the surjectivity of the divergence operator from $H(\mathrm{div},\Omega^p)$ onto $L^2(\Omega)$ and the inf-sup condition

$$\inf_{q\in L^2(\Omega^p)}\sup_{\boldsymbol{v}\in H(\mathrm{div},\Omega^p)}\frac{(q,\nabla\cdot\boldsymbol{v})_{\Omega^p}}{||\boldsymbol{v}||_{H(\mathrm{div},\Omega^p)}||q||_{L^2(\Omega^p)}} \geq \beta. \tag{13}$$

We denote with R_h, $R_{h,0}$ and Q_h^p two conforming FE approximations of $H(\mathrm{div},\Omega^p)$, $H_0(\mathrm{div},\Omega^p)$ and $L^2(\Omega^p)$ respectively. Using BDF1 for the time integration, the Galerkin approximation of this problem at the time step $n+1$ consists of: given $\boldsymbol{q}_h^n$, find $\boldsymbol{q}_h^{n+1} \in R_{h,0}$ and $p_{p,h}^{n+1} \in Q_h^p$ such that

$$\left(\frac{\rho_d}{\phi}\mathrm{d}_t\boldsymbol{q}_h^{n+1} + \kappa^{-1}\boldsymbol{q}_h^{n+1} + \nabla p_{p,h}^{n+1}, \boldsymbol{r}_h\right)_{\Omega^p} = (\boldsymbol{f}_d^{n+1}, \boldsymbol{r}_h)_{\Omega^p}, \tag{14a}$$

$$(\nabla\cdot\boldsymbol{q}_h^{n+1}, q_{p,h})_{\Omega^p} = (g^{n+1}, q_{p,h})_{\Omega^p}, \tag{14b}$$

for all $(\boldsymbol{r}_h, q_{p,h}) \in R_{h,0}\times Q_h^p$.

Only certain combinations of velocity and pressure interpolations are stable. The solution of (14) is unique provided the discrete counterpart of (13) is satisfied, i.e. there exists $\beta_d > 0$, independent of h, such that

$$\inf_{q_h\in Q_h^p}\sup_{\boldsymbol{v}_h\in R_h}\frac{(q_h,\nabla\cdot\boldsymbol{v}_h)_{\Omega^p}}{||\boldsymbol{v}_h||_{H(\mathrm{div},\Omega^p)}||q_h||_{L^2(\Omega^p)}} \geq \beta_d. \tag{15}$$

To circumvent this restriction, we adopt a residual-based stabilization technique. The idea is to introduce new terms in the formulation to provide stability without the need to

satisfy (15). The stabilized problem keeps consistency, since the stabilization terms are the broken product $(\cdot,\cdot)_K$ between the adjoint of the differential operator that defines the problem applied over the test function and the FE residual. This kind of methods can be heuristically motivated within the variational multiscale (VMS) frame, introduced in [40]. The key idea of the formulation is a multiscale splitting of the variable of interest into resolved (grid) scale and unresolved (subgrid) scales. This decomposition acknowledges that the smallest frequencies of the solution cannot be captured by the FE mesh. This approach has been successfully applied to a variety of problems (see, e.g., [41, 24, 58, 42, 26, 3, 2]).

Let us use the multiscale decomposition over the filtration velocity $\boldsymbol{q} = \boldsymbol{q}_h + \widetilde{\boldsymbol{q}}$ only. We refer to [3] for the stabilization of the Darcy problem with a multiscale decomposition of the pressure also. Using the same decomposition for the momentum conservation test function $\boldsymbol{r} = \boldsymbol{r}_h + \widetilde{\boldsymbol{r}}$, the subscale problem (the one tested against $\widetilde{\boldsymbol{r}}$) reads:

$$\left(\frac{\rho_d}{\phi}\mathrm{d}_t\widetilde{\boldsymbol{q}}^{n+1} + \kappa^{-1}\widetilde{\boldsymbol{q}}^{n+1}, \widetilde{\boldsymbol{r}}\right)_{\Omega^p} = \left(\boldsymbol{f}_d^{n+1} - \frac{\rho_d}{\phi}\mathrm{d}_t\boldsymbol{q}_h^{n+1} - \kappa^{-1}\boldsymbol{q}_h^{n+1} - \nabla p_{p,h}^{n+1}, \widetilde{\boldsymbol{r}}\right)_{\Omega^p}. \quad (16)$$

The FE equations (the ones tested against $(\boldsymbol{r}_h, q_{p,h})$) of the multiscale problem reads:

$$\left(\frac{\rho_d}{\phi}\mathrm{d}_t\boldsymbol{q}_h^{n+1} + \kappa^{-1}\boldsymbol{q}_h^{n+1} + \nabla p_{p_h}, \boldsymbol{r}_h\right)_{\Omega^p} + \left(\frac{\rho_d}{\phi}\mathrm{d}_t\widetilde{\boldsymbol{q}}^{n+1} + \kappa^{-1}\widetilde{\boldsymbol{q}}^{n+1}, \boldsymbol{r}_h\right)_{\Omega^p} = (\boldsymbol{f}_d^{n+1}, \boldsymbol{r}_h)_{\Omega^p} \quad (17a)$$

$$(\nabla\cdot\boldsymbol{q}_h^{n+1}, q_{p,h})_{\Omega^p} - (\widetilde{\boldsymbol{q}}^{n+1}, \nabla q_{p,h})_{\Omega^p} = (g^{n+1}, q_{p,h})_{\Omega^p}. \quad (17b)$$

The effect of the subscales in the FE problem is introduced by the subscale terms in the previous equations. The multiscale system (16)-(17) is as expensive as the continuum problem and is not numerically feasible. Thus, approximations have to be made. The subscale problem (16) must be replaced by a simplified model (the so-called modelling of the subscales) and plugged into the FE problem (17). A detailed description of this process can be found elsewhere, e.g. in [40, 27, 2]. The idea is to replace (16) by a simplified element-wise expression. Let us introduce some ingredients: given a function g such that $g|_K \in L^2(K)$ for any FE $K \in \mathcal{T}_h$ in Ω^p, the *broken* identity $\bar{I}$ is defined as $\bar{I}(g) = \sum_K g|_K$. The broken L^2-projection over a Hilbert space X, denoted by $\bar{\Pi}_X(g)$, is defined as the solution of:

$$\left(\bar{\Pi}_X(g), v\right) = \sum_K (g, v)_K, \qquad \forall v \in X.$$

Naturally, we define $\bar{\Pi}_X^{\perp}(g) = \bar{I}(g) - \bar{\Pi}_X(g) \in L^2(\Omega)$. The model for the subscales has the following form:

$$\frac{\rho_d}{\phi}\mathrm{d}_t\widetilde{\boldsymbol{q}}^{n+1} + \kappa^{-1}\widetilde{\boldsymbol{q}}^{n+1} = P_h\left(\boldsymbol{f}_d^{n+1} - \frac{\rho_d}{\phi}\mathrm{d}_t\boldsymbol{q}_h^{n+1} - \kappa^{-1}\boldsymbol{q}_h^{n+1} + \nabla p_{p,h}^{n+1}\right). \quad (18)$$

where P_h can be $\bar{I}$ (times a constant), leading to the algebraic subgrid scales (ASGS) method introduced in [40] or the orthogonal projection $\bar{\Pi}_{R_h}^{\perp}$, recovering the orthogonal subgrid scales (OSS) approach in [25, 27]. Another typical assumption is to neglect the subgrid time derivative in (16). The corresponding approach is called quasi-static subscales in [27]. As pointed out in [13] for the Stokes problem, this approximation can lead to instabilities when the small time step size goes to zero whereas the dynamic approach (i.e., the subgrid time derivative is not neglected) is shown to be stable for any value of the time step size [2, 28]. For the subsequent developments, we consider the ASGS and the dynamic OSS approach.

For the ASGS method, we have $P_h = \tau_d \bar{I}$, where $0 < \tau_d < 1$ is a positive constant. For instance, in [50] the authors have chosen $\tau_d = 1/2$. Invoking (18) in the momentum conservation equation (17a), we get

$$(1-\tau_d)\left(\frac{\rho_d}{\phi}\mathrm{d}_t \boldsymbol{q}_h^{n+1} + \kappa^{-1}\boldsymbol{q}_h^{n+1} + \nabla p_{p,h}^{n+1}, \boldsymbol{r}_h\right)_{\Omega^p} = (1-\tau_d)(\boldsymbol{f}_d^{n+1}, \boldsymbol{r}_h)_{\Omega^p}. \tag{19}$$

Apart from the singular choice $\tau_d = 1$, which cannot be made, the momentum conservation equation remains identical after stabilization. It implies that:

$$\frac{\rho_d}{\phi}\mathrm{d}_t \boldsymbol{q}_h^{n+1} + \kappa^{-1}\boldsymbol{q}_h^{n+1} = \bar{\Pi}_{R_h}(\boldsymbol{f}_d^{n+1} - \nabla p_{p,h}^{n+1}), \tag{20}$$

and

$$\frac{\rho_d}{\phi}\mathrm{d}_t \widetilde{\boldsymbol{q}}^{n+1} + \kappa^{-1}\widetilde{\boldsymbol{q}}^{n+1} = \tau_d \bar{\Pi}^{\perp}_{R_h}(\boldsymbol{f}_d^{n+1} - \nabla p_{p,h}^{n+1}). \tag{21}$$

By taking the time derivative of (14b) and combining it linearly with equation (14b) itself in order to exploit (20)-(21), we get

$$\begin{aligned}
&\left(\nabla\cdot\left(\frac{\rho_d}{\phi}\mathrm{d}_t \boldsymbol{q}_h^{n+1} + \kappa^{-1}\boldsymbol{q}_h^{n+1}\right), q_{p,h}\right)_{\Omega^p} - \left(\frac{\rho_d}{\phi}\mathrm{d}_t \widetilde{\boldsymbol{q}}^{n+1} + \kappa^{-1}\widetilde{\boldsymbol{q}}^{n+1}, \nabla q_{p,h}\right)_{\Omega^p} \\
&= \left(\frac{\rho_d}{\phi}\mathrm{d}_t g^{n+1} + \kappa^{-1} g^{n+1}, q_{p,h}\right)_{\Omega^p},
\end{aligned}$$

which leads to the stabilized mass conservation equation

$$\begin{aligned}
&(1-\tau_d)(\bar{\Pi}_{R_h}(\nabla p_{p,h}^{n+1}), \nabla q_{p,h})_{\Omega^p} + \tau_d(\nabla p_{p,h}^{n+1}, \nabla q_{p,h})_{\Omega^p} \qquad (22)\\
&= \left(\frac{\rho_d}{\phi}\mathrm{d}_t g^{n+1} + \kappa^{-1} g^{n+1}, q_{p,h}\right)_{\Omega^p} + (\bar{\Pi}_{R_h}(\boldsymbol{f}_d^{n+1}), \nabla q_{p,h})_{\Omega^p} + \tau_d(\bar{\Pi}^{\perp}_{R_h}(\boldsymbol{f}_d^{n+1}), \nabla q_{p,h})_{\Omega^p}.
\end{aligned}$$

Testing (19)-(22) against $(\boldsymbol{q}_h^{n+1}, p_{p,h}^{n+1})$, and adding up for all time steps $i = 0, ..., n$, we obtain the stability estimate

$$\left(\frac{\rho_d}{\phi\delta t}\right)||\boldsymbol{q}_h^{n+1}||^2_{L^2(\Omega^p)} + \kappa^{-1}\sum_{i=0}^{n}||\boldsymbol{q}_h^{i+1}||^2_{L^2(\Omega^p)} + \tau_d\sum_{i=0}^{n}||\nabla p_{p,h}^{i+1}||^2_{\Omega^p} \leq C(\boldsymbol{f}, g, \boldsymbol{q}_0) \tag{23}$$

where $C(\boldsymbol{f}, g, \boldsymbol{q}_0)$ is a positive constant that does depend on the data. It implies the well-possedness of the stabilized problem (19)-(22).

Remark 4.1 *Let us denote with M, G, D, and L the mass, gradient, divergence, and Laplacian matrices, respectively. Let us consider the steady-state problem, by switching off all the time derivatives in (19)-(22) . The Galerkin approximation of the primal formulation requires the solution of system*

$$L\mathbf{P} = \kappa^{-1}\mathbf{G} - D\mathbf{F}_d, \tag{24}$$

where $\mathbf{P}$, $\mathbf{G}$, and $\mathbf{F}_d$ are the arrays of nodal values for pressure, g, and $\boldsymbol{f}_d$. On the other side, the Galerkin mixed formulation leads to the pressure Poisson equation

$$(-DM^{-1}G)\mathbf{P} = \kappa^{-1}\mathbf{G} - DM^{-1}\mathbf{F}_d. \tag{25}$$

System matrix $(-DM^{-1}G)$ is a non-standard discrete Laplacian, that is non-singular only for FE spaces satisfying the inf-sup condition (15). The algebraic formulation of the steady-state stabilized problem is

$$((1-\tau_d)(-DM^{-1}G) + \tau_d L)\mathbf{P} = \kappa^{-1}\mathbf{G} - \tau_d D\mathbf{F}_d - (1-\tau_d)DM^{-1}\mathbf{F}_d,$$

which is a linear combination of (24) and (25). For the transient problem, the algebraic form of equation (22) is

$$((1-\tau_d)(-DM^{-1}G)+\tau_d L)\mathbf{P}^{n+1} = \frac{\rho_d}{\phi}\mathrm{d}_t\mathbf{G}^{n+1}+\kappa^{-1}\mathbf{G}^{n+1}-\tau_d D\mathbf{F}_d-(1-\tau_d)DM^{-1}\mathbf{F}_d$$

The system matrix is unchanged with respect to the steady case.

Remark 4.2 *The OSS method is obtained by using $P_h = \tau_d\bar{\Pi}^{\perp}_{R_h}$. It is easy to infer that ASGS and OSS are equivalent for the Darcy problem when $\tau_d \neq 1$. Unlike ASGS, OSS can use $\tau_d = 1$.*

Remark 4.3 *In case of using a quasi-static approach, that is to say, eliminating the subgrid time derivatives, the OSS stabilized problem is much simpler. It consists of Galerkin system (14), adding the pressure stabilization term $\tau_d(\bar{\Pi}_{R_h}(\nabla p^{n+1}_{p,h}), \nabla q_{p,h})$ to the left hand side of (14b).*

4.2. Stabilization of incompressible elasticity

We could consider a stabilized FE approximation of the Biot system in which we would only stabilize the Darcy subproblem, i.e. simply adding the stabilization terms due to the multiscale decomposition of $\boldsymbol{q}_h$. Unfortunately, this approach would not work in case the conductivity goes to zero and the porous matrix is incompressible. The hydraulic conductivity κ (the ratio between the permeability and the viscosity) of a human artery has been evaluated experimentally in [70] and used for applications in [71, 59]. Realistic values are $\kappa \sim 10^{-12}$ (cm^3 s)/g. For those values of hydraulic conductivity, the orders of magnitude of the two velocities $\boldsymbol{u}_s$ and $\boldsymbol{q}$ are very different. We could say that the Biot problem for hemodynamics is closer to the limit problem of an impervious structure. Therefore, the approach reported in the previous subsection is not enough in hemodynamics.

In order to get a stabilized Biot system in both limits, we have to design a stabilized method for incompressible elasticity. We focus on the OSS approach, since OSS and ASGS are different in this case. Let us consider an incompressible structure that occupies Ω^p in the reference configuration and homogeneous boundary conditions. V_h, $V_{h,0}$ and Q^p_h are conforming FE approximations of $H^1(\Omega^p)^d$, $H^1_0(\Omega^p)^d$, and $L^2(\Omega^p)$, respectively. We choose the BDF1 scheme for the time discretization. Let us omit the time subscript in the moving domain for conciseness. The Galerkin approximation of the simplified problem written in terms of structure displacement $\boldsymbol{\eta}_h$ reads: given $\boldsymbol{\eta}^n_h$ and $\boldsymbol{\eta}^{n-1}_h$, for $n \geq 0$ find $\boldsymbol{\eta}^{n+1}_h \in V^s_{0,h}$ and $p^{n+1}_{p,h} \in Q^p_h$ such that

$$\begin{aligned}\rho_p\left(\mathrm{d}_{tt}\boldsymbol{\eta}^{n+1}_h, \boldsymbol{v}^s_h\right)_{\Omega^p} + \left(\boldsymbol{\sigma}^{\mathrm{dev}}_s(\boldsymbol{\eta}^{n+1}_h), \nabla\boldsymbol{v}^s_h\right)_{\Omega^p} - (p^{n+1}_{p,h}, \nabla\cdot\boldsymbol{v}^s_h)_{\Omega^p} &= (\boldsymbol{f}^{n+1}_s, \boldsymbol{v}^s_h)_{\Omega^p},\\ (\nabla\cdot\boldsymbol{\eta}^{n+1}_h, q_{p,h})_{\Omega^p} &= (g^{n+1}, q_{p,h})_{\Omega^p}, \quad (26)\end{aligned}$$

for all $(\boldsymbol{v}^s_h, q_{p,h}) \in V^s_{0,h} \times Q^p_h$. We assume that $\boldsymbol{\eta}^0_h \in V^s_{0,h}$ and $(\nabla\cdot\boldsymbol{\eta}^0_h, q_{p,h})_{\Omega^p} = (g^0, q_{p,h})_{\Omega^p}$.

Let us take $\boldsymbol{\sigma}^{\mathrm{dev}}_s(\boldsymbol{\eta}^{n+1}_h) = \mu_\ell\nabla\boldsymbol{\eta}$. We employ the quasi-static subscales for $\boldsymbol{\eta}$ to circumvent the necessity of conforming finite elements. Invoking the decomposition into FE approximation and subgrid scale for both $\boldsymbol{\eta}^{n+1}$ and $\boldsymbol{v}^s$, we get the subscale problem:

$$\begin{aligned}&\left(\rho_d\mathrm{d}_{tt}\widetilde{\boldsymbol{\eta}}^{n+1} - \nabla\cdot\boldsymbol{\sigma}^{\mathrm{dev}}_s(\widetilde{\boldsymbol{\eta}}^{n+1}), \widetilde{\boldsymbol{v}}^s\right)_{\Omega^p}\\ &= \left(\boldsymbol{f}^{n+1}_s - \rho_p\mathrm{d}_{tt}\boldsymbol{\eta}^{n+1}_h + \nabla\cdot\boldsymbol{\sigma}^{\mathrm{dev}}_s(\boldsymbol{\eta}^{n+1}_h) - \nabla p_h, \widetilde{\boldsymbol{v}}^s\right)_{\Omega^p}. \quad (27)\end{aligned}$$

Two approximations are required in (26) in order to find an expression for the subscale $\widetilde{\boldsymbol{\eta}}^{n+1}$ in terms of $(\boldsymbol{\eta}_h^{n+1}, p_{p,h}^{n+1})$. The differential operator applied over $\widetilde{\boldsymbol{\eta}}^{n+1}$ can be simplified at every finite element as

$$-\nabla\cdot\boldsymbol{\sigma}_s^{\mathrm{dev}}(\widetilde{\boldsymbol{\eta}}^{n+1}) \approx \tau_s^{-1}\widetilde{\boldsymbol{\eta}}^{n+1}, \tag{28}$$

using Fourier analysis (see [26, 22, 2]). Here τ_s is the stabilization parameter defined within each element

$$\tau_s = c\left(\frac{2\mu_\ell}{h^2}\right)^{-1},$$

where c is an algorithmic constant and h is a characteristic length of the element. As for the Darcy problem, we can use approximation (28) and derive the model for the subscale

$$\rho_d \mathrm{d}_{tt}\widetilde{\boldsymbol{\eta}}^{n+1} + \tau_s^{-1}\widetilde{\boldsymbol{\eta}}^{n+1} = P_h\left(\boldsymbol{f}_s^{n+1} - \rho_p \mathrm{d}_{tt}\boldsymbol{\eta}_h^{n+1} + \nabla\cdot\boldsymbol{\sigma}_s^{\mathrm{dev}}(\boldsymbol{\eta}_h^{n+1}) - \nabla p_h\right). \tag{29}$$

The FE subproblem of the multiscale system reads as:

$$\rho_p\left(\mathrm{d}_{tt}\boldsymbol{\eta}_h^{n+1}, \boldsymbol{v}_h^s\right)_{\Omega^p} + \left(\boldsymbol{\sigma}_s^{\mathrm{dev}}(\boldsymbol{\eta}_h^{n+1}), \nabla\boldsymbol{v}_h^s\right)_{\Omega^p} - \sum_K\left(\widetilde{\boldsymbol{\eta}}^{n+1}, \boldsymbol{\sigma}_{s,h}^{\mathrm{dev}*}(\nabla\boldsymbol{v}_h^s)\right)_K$$
$$- (p_{p,h}^{n+1}, \nabla\cdot\boldsymbol{v}_h^s)_{\Omega^p} = (\boldsymbol{f}_s^{n+1}, \boldsymbol{v}_h^s)_{\Omega^p}, \tag{30a}$$

$$(\nabla\cdot\boldsymbol{\eta}_h^{n+1}, q_{p,h})_{\Omega^p} - \sum_K(\widetilde{\boldsymbol{\eta}}^{n+1}, \nabla q_{p,h})_K = (g^{n+1}, q_{p,h})_{\Omega^p}, \tag{30b}$$

where the stabilization terms (those that depend on the subgrid solution) are replaced by broken integrals over finite elements, neglecting inter-element jumps. Together with the model of the subscales, this is the other approximation usually used in VMS-based stabilization techniques (see, e.g., [2]). The terms $\nabla\cdot\boldsymbol{\sigma}_s^{\mathrm{dev}}(\boldsymbol{\eta}_h^{n+1})$ and $\boldsymbol{\sigma}_{s,h}^{\mathrm{dev}*}(\nabla\boldsymbol{v}_h^s)$ involve second derivatives of FE functions which will vanish in case of linear elements. The stabilized problem is obtained by invoking (29) in (30a). In case of using the quasi-static approximation, the situation is slightly simpler, since $\mathrm{d}_{tt}\widetilde{\boldsymbol{\eta}}^{n+1}$ is neglected in (29) and (30). Thus, (29) becomes a closed form of the subscale in terms of the FE components. This closed form can be plugged in (30), obtaining the stabilized problem in terms of the FE components only. Thus, for quasi-static subscales, the subscales do not need to be stored and tracked in time. This approach clearly simplifies the stabilized algorithm and reduces the memory requirements. The price to pay is the loss of stability for anisotropic space-time approximations (see [28, 2] for a detailed discussion of this topic). As far as we know, this is the first time that a dynamic stabilization has been presented for transient incompressible elasticity.

4.3. The stabilized Biot system

We have shown how to stabilize the Darcy problem and the incompressible elasticity separately. Now, our goal is to stabilize the Biot system in such a way that the stabilized algorithm will remain stable in both limits of this problem. Thus, we have to combine the algorithms in subsections 4.1-4.2. We consider again the VMS approach, with multiscale decomposition for both $\boldsymbol{u}^s$ and $\boldsymbol{q}$ (and the respective test functions). We omit the details, since the process is identical as above, but with many more terms. Using the modelling assumptions over the subscale equations for $\widetilde{\boldsymbol{u}}_s^{n+1}$ and $\widetilde{\boldsymbol{q}}^{n+1}$, we get the following stabilized problem: given $\boldsymbol{u}_{s,h}^n$ and $\boldsymbol{q}_h^n$, compute $\boldsymbol{u}_{s,h}^{n+1}$, $\boldsymbol{q}_h^{n+1}$, $p_{p,h}^{n+1}$ such

that

$$
\begin{aligned}
&\rho_p(\mathrm{d}_t\boldsymbol{u}_{s,h}^{n+1},\boldsymbol{v}_h^s)_{\Omega^p}+\rho_d(\mathrm{d}_t\boldsymbol{q}_h^{n+1},\boldsymbol{v}_h^s)_{\Omega^p}+(\boldsymbol{\sigma}_s^{\mathrm{dev}}(\boldsymbol{\eta}_h^{n+1}),\nabla\boldsymbol{v}_h^s)_{\Omega^p}-\left(p_{p,h}^{n+1},\nabla\cdot\boldsymbol{v}_h^s\right)_{\Omega^p}\\
&+\rho_d(\mathrm{d}_t\boldsymbol{u}_{s,h}^{n+1},\boldsymbol{r}_h)_{\Omega_t^p}+\frac{\rho_d}{\phi}(\mathrm{d}_t\boldsymbol{q}_h^{n+1},\boldsymbol{r}_h)_{\Omega^p}+\kappa^{-1}(\boldsymbol{q}_h^{n+1},\boldsymbol{r}_h)_{\Omega^p}-(p_{p,h}^{n+1},\nabla\cdot\boldsymbol{r}_h)_{\Omega^p}\\
&+(\nabla\cdot(\boldsymbol{u}_{s,h}^{n+1}+\boldsymbol{q}_h^{n+1}),q_{p,h}^{n+1})_{\Omega^p}\\
&+\sum_K\left(\rho_p\mathrm{d}_t\widetilde{\boldsymbol{u}}_s^{n+1}+\rho_d\mathrm{d}_t\widetilde{\boldsymbol{q}}^{n+1},\boldsymbol{v}_h^s\right)_K+\sum_K\left(\widetilde{\boldsymbol{\eta}}_s^{n+1},\boldsymbol{\sigma}_s^{\mathrm{dev}*}(\nabla\boldsymbol{v}_h^s)\right)_K\\
&+\sum_K\left(\rho_d\mathrm{d}_t\widetilde{\boldsymbol{u}}_s^{n+1}+\frac{\rho_d}{\phi}\mathrm{d}_t\widetilde{\boldsymbol{q}}^{n+1}+\kappa^{-1}\widetilde{\boldsymbol{q}}^{n+1},\boldsymbol{r}_h\right)_K-\sum_K\left(\widetilde{\boldsymbol{u}}_s^{n+1}+\widetilde{\boldsymbol{q}}^{n+1},\nabla q_{p,h}\right)_K\\
&=\langle\boldsymbol{f}_s,\boldsymbol{v}_h^s\rangle_{\Omega^p}+\langle\boldsymbol{f}_d,\boldsymbol{r}_h\rangle_{\Omega^p}
\end{aligned}
\tag{31}
$$

for any $(\boldsymbol{v}_h,\boldsymbol{r}_h,q_{p,h})V_{h,0}\in R_{h,0}\times Q_h^p$. The stabilization terms are those in the fourth and fifth line of (31). Analogously, the models for the subscales are:

$$
\begin{aligned}
&\rho_p\mathrm{d}_t\widetilde{\boldsymbol{u}}_s^{n+1}+\rho_d\mathrm{d}_t\widetilde{\boldsymbol{q}}^{n+1}+\tau_s^{-1}\widetilde{\boldsymbol{\eta}}^{n+1}\\
&=P_{V_h}\left(\boldsymbol{f}_s^{n+1}-\rho_p\mathrm{d}_t\boldsymbol{u}_{s,h}^{n+1}-\rho_d\mathrm{d}_t\boldsymbol{q}_h^{n+1}-\nabla\cdot\boldsymbol{\sigma}_s^{\mathrm{dev}}(\boldsymbol{\eta}_h^{n+1})-\nabla p_{p,h}^{n+1}\right),\\
&\rho_d\mathrm{d}_t\widetilde{\boldsymbol{u}}_s^{n+1}+\rho_d\phi^{-1}\mathrm{d}_t\widetilde{\boldsymbol{q}}^{n+1}+\kappa^{-1}\widetilde{\boldsymbol{q}}^{n+1}\\
&=P_{R_h}\left(\boldsymbol{f}_d^{n+1}-\rho_d\mathrm{d}_t\boldsymbol{u}_{s,h}^{n+1}-\rho_d\phi^{-1}\mathrm{d}_t\boldsymbol{q}_h^{n+1}-\kappa^{-1}\boldsymbol{q}_h^{n+1}-\nabla p_{p,h}^{n+1}\right).
\end{aligned}
\tag{32}
$$

This stabilized algorithm is complicated and the subscale unknowns $\widetilde{\boldsymbol{u}}_s^{n+1}$ and $\widetilde{\boldsymbol{q}}^{n+1}$ in (32) are coupled. In order to simplify the method, let us consider the quasi-static approach, OSS, equal interpolation for $\boldsymbol{u}_{h,s}$ and $\boldsymbol{q}_{h,s}$ with linear Lagrangian elements and $\bar{\Pi}_{V_h}^{\perp}(\boldsymbol{f}_s)=\bar{\Pi}_{V_h}^{\perp}(\boldsymbol{f}_d)=0$. In this case, the subscale equations (32) reduces to:

$$
\begin{aligned}
\tau_s^{-1}\widetilde{\boldsymbol{\eta}}^{n+1}&=-\bar{\Pi}_{V_h}^{\perp}\left(\nabla p_{p,h}^{n+1}\right),\\
\tau_d^{-1}\kappa^{-1}\widetilde{\boldsymbol{q}}^{n+1}&=-\bar{\Pi}_{V_h}^{\perp}\left(\nabla p_{p,h}^{n+1}\right),
\end{aligned}
\tag{33}
$$

and the stabilized Biot system reduces to

$$
\begin{aligned}
&\rho_p(\mathrm{d}_t\boldsymbol{u}_{s,h}^{n+1},\boldsymbol{v}_h^s)_{\Omega^p}+\rho_d(\mathrm{d}_t\boldsymbol{q}_h^{n+1},\boldsymbol{v}_h^s)_{\Omega^p}+(\boldsymbol{\sigma}_s^{\mathrm{dev}}(\boldsymbol{\eta}_h^{n+1}),\nabla\boldsymbol{v}_h^s)_{\Omega^p}-\left(p_{p,h}^{n+1},\nabla\cdot\boldsymbol{v}_h^s\right)_{\Omega^p}\\
&+\rho_d(\mathrm{d}_t\boldsymbol{u}_{s,h}^{n+1},\boldsymbol{r}_h)_{\Omega_t^p}+\frac{\rho_d}{\phi}(\mathrm{d}_t\boldsymbol{q}_h^{n+1},\boldsymbol{r}_h)_{\Omega^p}+\kappa^{-1}(\boldsymbol{q}_h^{n+1},\boldsymbol{r}_h)_{\Omega^p}-(p_{p,h}^{n+1},\nabla\cdot\boldsymbol{r}_h)_{\Omega^p}\\
&+(\nabla\cdot(\boldsymbol{u}_{s,h}^{n+1}+\boldsymbol{q}_h^{n+1}),q_{p,h}^{n+1})_{\Omega^p}+\sum_K(\tau_s+\tau_d\kappa)\left(\bar{\Pi}_{V_h}^{\perp}\left(\nabla p_{p,h}^{n+1}\right),\nabla q_{p,h}\right)_K\\
&=\langle\boldsymbol{f}_s,\boldsymbol{v}_h^s\rangle_{\Omega^p}+\langle\boldsymbol{f}_d,\boldsymbol{r}_h\rangle_{\Omega^p}
\end{aligned}
\tag{34}
$$

The stabilization has been drastically reduced to the second term in the third row. The previous approximations do not hold in general. Anyway, the OSS technique loses consistency but it is not a problem since it does not spoil accuracy (see, e.g., [1]).

5. The linear fluid-structure system

Let us start with the linearization of the coupled problem. Due to the fact that the Navier-Stokes equations are non-linear, we can use either a fixed point or Newton method, that introduces nonlinearity iterations. The fixed point method simply replaces

the convective velocity with the one of the previous iteration. In FSI, the coupled problem is defined over a moving domain. Thus, we must linearize with respect to the domain too. We have used a fixed point linearization for both nonlinearities and considered semi-implicit algorithms (nonlinearities are explicitly treated). We omit here the details and refer to [36, 8] for a detailed exposition. We also refer to [37] for a full Newton linearization in the frame of FSI.

Once problem (10) is discretized in space and time and linearized by a fixed point method, we are able to write the linear system that has to be solved at every fixed point iteration. The purpose of this section is to write this system.

In order to simplify the exposition, let us consider that $V_h^f(t^{n+1})$, $V_h^s(t^{n+1})$, and $R_h(t^{n+1})$ are built with the same FE type. In particular, we consider Lagrange finite elements. At a node a, we can define the scalar nodal test function ϕ_a. Since we are dealing with vectorial fields, we have to extend the scalar test functions to the vectorial case. We denote by $\boldsymbol{\phi}_a^i$ the vectorial test function associated to node a and component i of the solution; all the components are zero, except the one for the i-th component, that takes the value ϕ_a, that is to say, the m-th component of this vectorial test function is $(\boldsymbol{\phi}_a^i)_m = \phi_a \delta_{im}$, where δ denotes the Kronecker delta. The pressure spaces $Q_h^f(t^{n+1})$, and $Q_h^p(t^{n+1})$ are spanned by test functions π_b, where b can be a node label for Lagrangian test functions or an element label for piecewise constant pressures. In fact, our stabilized formulation allows to use the same Lagrangian basis for the pressure too, and this is our choice in the numerical experiments.

The sets of fluid and structure inner nodes are denoted by $\mathcal{N}_f$ and $\mathcal{N}_s$, respectively. The set of nodes on the interface are denoted by $\mathcal{N}_\sigma$. Thus, $V_h^f(t^{n+1})$ is spaned by $\{\boldsymbol{\phi}_a^i\}_{a\in\mathcal{N}_f} \oplus \left\{\boldsymbol{\phi}_b^i|_{\Omega^f_{t^{n+1}}}\right\}_{b\in\mathcal{N}_\sigma}$, where $\boldsymbol{\phi}_b^i|_{\Omega^f_{t^{n+1}}}$ denotes the restriction of the function over $\Omega^f_{t^{n+1}}$; analogously for V_h^s and R_h over Ω_t^p. Pressure nodes in the fluid and structure subdomain are indicated by $\mathcal{N}_{pf}$ and $\mathcal{N}_{pp}$. We focus on the case of geometrical conforming grids, so the nodes $\mathcal{N}_\sigma$ belong to the grids of both subdomains. For every interface node we can define the tangential and normal vectors with respect to $\Sigma_{t^{n+1}}$. Then, we can rotate the test (and trial) test functions to this nodal coordinate system.

Let us omit the time superscript in the arrays of unknowns for clarity. The terms involving values from previous time steps will be included in the right-hand side. We denote the arrays of nodal values of $\boldsymbol{u}_{f,h}^{n+1}$, $\boldsymbol{u}_{s,h}^{n+1}$, and $\boldsymbol{q}_h^{n+1}$ with $\mathbf{U}_f^f$, $\mathbf{U}_s^s$, and $\mathbf{Q}_s$, respectively. The arrays $\mathbf{U}_\sigma^f$, $\mathbf{U}_\sigma^s$, and $\mathbf{Q}_\sigma$ are related to the interface nodes. For interface nodes, it is convenient to rotate the interface arrays from the global coordinate system to the tangent-normal system (defined at every node). We denote by T the rotation matrix from the local tangent-normal systems to the global system; T^T is the inverse rotation, where ^{T} indicates the tranpose. The rotated interface arrays are denoted by $\tilde{\mathbf{U}}_\sigma^f$, $\tilde{\mathbf{U}}_\sigma^s$, and $\tilde{\mathbf{Q}}_\sigma$. These arrays are composed by tangent and normal components of the velocities at all the nodes in $\mathcal{N}_\sigma$. $\mathbf{P}^f$ and $\mathbf{P}^p$ are the arrays of nodal values for the pressure in Ω_t^f and Ω_t^p, respectively.

In order to write the fully discretized coupled problem for a given time value t^{n+1}, we need to define a set of matrices. The mass matrix is denoted by $M_{\alpha\beta}^\delta$ where the subindexes α and β indicate the position of fluid nodes: the "value" σ is used for nodes on Σ_t, f ar s otherwise. Since there are mass matrices in both subdomains, we need the subscript δ to specify the subdomain ($\delta = f$ or $\delta = s$). Using the same notation, we denote by $K_{\alpha\beta}$ the matrix that includes the viscous and convective terms, as well as the corresponding stabilization terms. Thus, the whole fluid matrix is denoted by $C_{\alpha\beta} = \frac{\rho_f}{\delta t} M_{\alpha\beta}^f + K_{\alpha\beta}$. The stabilized gradient matrix is denoted by G_β^δ, δ corresponding to the subdomain and β to the set of nodes. The stabilized divergence matrix is D_β^δ. Using this notation, we indicate with L_τ^δ the Laplacian matrix associated to the pressure

stabilization (τ denotes the fact that this matrix is a Laplacian times the stabilization parameter). For the Biot system, let us denote with $N_{\alpha\beta}$ the matrix related to the structural velocity (or displacement) in (34) as well as the corresponding stabilization terms.

With these ingredients, we can write the algebraic fluid subproblem for inner velocity test functions $\{\boldsymbol{\phi}_a^i\}_{a\in\mathcal{N}_f}$ and pressure test functions $\{\pi_a\}_{a\in\mathcal{N}_{pf}}$:

$$\begin{aligned} C_{ff}\mathbf{U}_f^f + C_{f\sigma}T\tilde{\mathbf{U}}_\sigma^f + G_f^f\mathbf{P}_f &= \mathbf{b}_f^f, \\ D_f^f\mathbf{U}_f^f + D_\sigma^f T\tilde{\mathbf{U}}_\sigma^f + L_\tau^f\mathbf{P}_f &= \mathbf{b}_p^f. \end{aligned} \tag{35}$$

The right-hand-side terms account for body forces, time integration and stabilization terms, and the structure terms related to the fact that the structure equation is stated in terms of velocities. Matrices $C_{f\sigma}$ and D_σ^f are multiplied by the rotation matrix T.

Testing (34) against inner structure test functions $\{\boldsymbol{\phi}_a\}_{a\in\mathcal{N}_s}$ (since V_h^s and R_h are built with the same FE type) and pressure test functions $\{\pi_a\}_{a\in\mathcal{N}_{pp}}$ we get the discrete equations:

$$\begin{aligned} N_{ss}\mathbf{U}_s^s + N_{s\sigma}T\tilde{\mathbf{U}}_\sigma^s + bM_{ss}^s\mathbf{Q}_s + bM_{s\sigma}^s T\tilde{\mathbf{Q}}_\sigma + G_s^s\mathbf{P}_s &= \mathbf{b}_s^s, \\ aM_{ss}^s\mathbf{Q}_s + aM_{s\sigma}^s T\tilde{\mathbf{Q}}_\sigma + bM_{ss}^s\mathbf{U}_s^s + bM_{s\sigma}^s T\tilde{\mathbf{U}}_\sigma^s + G_s^s\mathbf{P}_s &= \mathbf{b}_d^s, \\ D_s^s\mathbf{U}_s^s + D_\sigma^s T\tilde{\mathbf{U}}_\sigma^s + D_s^s\mathbf{Q}_s + D_\sigma^s T\tilde{\mathbf{Q}}_\sigma + L_\tau^s\mathbf{P}_s &= \mathbf{b}_p^s, \end{aligned} \tag{36}$$

where we have used $a = (\rho_d(\delta t\phi)^{-1} + \kappa^{-1})$ and $b = \rho_d\delta t^{-1}$. $R_{h,0}$ includes functions with null normal trace, those with non-zero tangential trace that have not been used yet. Now, we test (34) against these interface test functions. This can be done by using the rotation matrix T^T. Since we are only interested in functions with zero normal trace, we use the matrix $T_{\boldsymbol{t}}^T$ that takes arrays in the global system and gives the tangential component only in the local tangent-normal system. We get:

$$T_{\boldsymbol{t}}^T\left(aM_{\sigma s}^s\mathbf{Q}_s + aM_{\sigma\sigma}^s T\tilde{\mathbf{Q}}_\sigma + bM_{\sigma s}^s\mathbf{U}_s^s + M_{\sigma\sigma}^s T\tilde{\mathbf{U}}_\sigma^s + G_\sigma^s\mathbf{P}_s\right) = T_{\boldsymbol{t}}^T\mathbf{b}_d^\sigma. \tag{37}$$

Equations (36)-(37) are the algebraic version of (10b). Now, we have to write the algebraic form of the transmission conditions (10c)-(10d). For matching grids, the space of traces for FE functions in V_h^f and V_h^s are identical. This space is simply $\{\boldsymbol{\phi}_a^i|_{\Sigma_t}\}_{a\in\mathcal{N}_\sigma}$. Using the extensions $\mathcal{E}_t^f(\boldsymbol{\phi}_a^i|_{\Sigma_t}) = \boldsymbol{\phi}_a^i|_{\Omega_t^f}$ and $\mathcal{E}_t^p(\boldsymbol{\phi}_a^i|_{\Sigma_t}) = \boldsymbol{\phi}_a^i|_{\Omega_t^p}$, it is easy to see that the algebraic counterpart of the continuity of total stresses (10c) is

$$\begin{aligned} &C_{\sigma f}\mathbf{U}_f^f + C_{\sigma\sigma}T\tilde{\mathbf{U}}_\sigma^f + G_\sigma^f\mathbf{P}_f \\ &+ N_{\sigma s}\mathbf{U}_s^s + N_{\sigma\sigma}T\tilde{\mathbf{U}}_\sigma^s + bM_{\sigma s}^s\mathbf{Q}_s + bM_{\sigma\sigma}^s T\tilde{\mathbf{Q}}_\sigma + G_\sigma^s\mathbf{P}_s = \mathbf{b}_\sigma^f + \mathbf{b}_\sigma^s. \end{aligned} \tag{38}$$

Let us define the interface matrix $(M_\Sigma)_{ab}^{ij} = (\boldsymbol{\phi}_a^i, \boldsymbol{\phi}_b^j)_{\Sigma_t}$ for $a, b \in \mathcal{N}_\sigma$. We also denote by $T_{\boldsymbol{t}}^*$ the matrix that takes an array of interface values in the tangent-normal system and gives the rotated values in the global system for the tangent component only (and zero elsewhere). This matrix is needed for the imposition of the Beavers-Joseph-Saffman condition (4d). The algebraic version of the continuity of stresses in (10d) is:

$$\begin{aligned} &C_{\sigma f}\mathbf{U}_f^f + C_{\sigma\sigma}T\mathbf{U}_\sigma^f + G_\sigma^f\mathbf{P}_f + aM_{\sigma s}\mathbf{Q}_s + aM_{\sigma\sigma}T\tilde{\mathbf{Q}}_\sigma \\ &+ bM_{\sigma s}\mathbf{U}_s^s + bM_{\sigma\sigma}T\mathbf{U}_\sigma^s + G_\sigma^s\mathbf{P}_s + cM_\Sigma T_{\boldsymbol{t}}^*\tilde{\mathbf{U}}_\sigma^f - cM_\Sigma T_{\boldsymbol{t}}^*\tilde{\mathbf{U}}_\sigma^s = \mathbf{b}_\sigma^f + \mathbf{b}_\sigma^d. \end{aligned} \tag{39a}$$

where $c = \gamma/\sqrt{\kappa}$. Finally, with the interface velocities in the normal-tangential system, it is easy to impose the continuity of normal velocities:

$$M_\Sigma T_{\boldsymbol{n}}\left(\tilde{\mathbf{U}}_\sigma^f - \tilde{\mathbf{U}}_\sigma^s - \tilde{\mathbf{Q}}_\sigma\right) = 0. \tag{40}$$

The algebraic Navier-Stokes coupled problem is composed by (36)-(40). All these equations can be included in a linear system

$$A\mathbf{X}^{n+1} = \mathbf{b}^{n+1}, \tag{41}$$

where $\mathbf{X}^{n+1}$ includes all the arrays of unknowns defined above. We refer to [35] for a detailed discussion about implementation aspects related to rotation matrices for imposition of boundary conditions.

Remark 5.1 *In case we use inf-sup stable finite elements for the fluid subproblem, submatrix L_τ^f is 0.*

Remark 5.2 *We have considered a 2d problem for the sake of simplicity. In a 3d case, we would transform variables and matrices from the Cartesian coordinate system x-y-z to the tangent-normal-binormal system. Details about this rotation can be found in [35].*

6. The monolithic approach

We have ended up with a linear system of equations (41) coupling all the unknowns of the Navier-Stokes/Biot problem. The first option we consider is a monolithic approach in which we use efficient preconditioners and solvers to the whole coupled system (41).

In hemodynamics problems, fluid and structural densities are of the same order, making the added-mass effect [20] critical and the solution of the coupled problem extremely challenging. Typical domain decompositions approaches fail to converge (see Section 7). For these reasons, in [7] we have considered a monolithic approximation of FSI problems with large added-mass effect. Those methods are non-modular in the sense that independent fluid and structural codes cannot be used as black boxes. However, the efficiency of the non-modular algorithms justify their use for hemodynamics applications.

Thus, the first approach we take into consideration for the solution of system (41) is the monolithic one. Let us summarize the main features of this formulation. We make use of conforming grids and the same finite element space for fluid and structure velocities. Moreover, since we adopt a stabilized formulation for the poroelastic structure, the same finite element interpolation space can be used for pressure p_p. In case of using stabilized finite elements for the fluid, we can use the same space for pressure p_f, too.

Thanks to these choices, the continuity of the stresses is easily imposed. As we have shown in Section 5, the weak transmission of stresses arises from the fact that the shape functions on the interface nodes have a support on both fluid and structure subdomains. The remaining coupling conditions, i.e. the admissibility condition and the Beavers-Joseph-Saffman condition, are easily enforced, once the interface mass matrix M_Σ is computed (see (39)).

We recall the solver used in [7] for the monolithic FSI problem. First we apply a scaling over (41), due to the different order of magnitude of the contributions related to every subproblem. This scaling has to adimensionalize the residual. The scaled problem reads:

$$\hat{A}\mathbf{X}^{n+1} = \hat{\mathbf{b}}^{n+1}$$

where we denote by D^{-1} the scaling matrix, $\hat{A} := D^{-1}A$ and $\hat{\mathbf{b}}^{n+1} := D^{-1}\mathbf{b}^{n+1}$. For stabilized fluid and Biot systems, this matrix is simply the diagonal of A. When the fluid problem is solved by using inf-sup stable elements, we can use an adimensionalization motivated by the pressure Schur complement; e.g. the scaling would be $(\mu_f h^2)^{-1}$ for the Stokes problem.

Over the scaled problem, we have used an ILUT preconditioner and the preconditioned system has been solved by a matrix-free Krylov method (see [62]). This methodology, that we will denote as the ILUT-solver approach, has been used for FSI problems in [7] with good results.

At time step t^{n+1}, the stopping criterion for the iterative procedure is based on the relative residual:

$$\frac{||\boldsymbol{r}^{k+1}||}{||\mathbf{b}^{n+1}||} = \frac{||\mathbf{b}^{n+1} - A\mathbf{X}^{n+1,k+1}||}{||\mathbf{b}^{n+1}||} < \epsilon. \tag{42}$$

The monolithic approach solves a problem whose size is bigger than those of the two subproblems. However, it has the advantage of robustness, in particular when the added-mass effect is critical (see Section 8.3).

Remark 6.1 *The monolithic approach with ILUT preconditioners is still interesting when parallel solvers are used. In fact, we can split the FSI domain into subdomains and use domain decomposition (DD) methods for the coupling of these subdomains. If subdomain interfaces do not coincide with fluid-structure interfaces, every subproblem can be solved using a monolithic approach.*

7. The domain decomposition approach

Alternatives to the monolithic approach are the so-called partitioned procedures. Fluid and structure subproblems are solved separately and coupled via transmission conditions in an iterative fashion. For aeroelastic applications (with negligible added-mass effect), these methods are a good choice, since the coupling can be treated explicitly without compromising stability. However, in case of large added-mass effects explicit methods are unstable. The remedy is to use implicit coupling methods, whose performance deteriorates as the added-mass effect gets large (see [57]).

Partitioned procedures are heterogeneous DD methods. The classical Dirichlet-Neumann (DN) method is just one of these procedures, but there are many others. The Neumann-Dirichlet (ND) and the Neumann-Neumann (NN) algorithms have already been proposed for hemodynamics problems [31]. None of those two clearly outperforms the DN method. Recently, partitioned procedures based on Robin transmission conditions have been succesfully applied to large-added mass effect problems in [5, 6]. We remind that all the domain decomposition algorithms can be interpreted as preconditioners over the interface problem (in terms of interface unknowns only). Depending on the iterative solver applied over the preconditioned system, we get different methods. Tipically, Richardson iterations are performed. These iterations are non-normal and convergence is not attained in general, requiring relaxation techniques (see [53]). More efficient Krylov solvers, like GMRES, perform orthonormal iterations that improve the convergence (see [37, 52, 6]). For simplicity, at the moment we do not consider the possibility of replacing Richardson iterations with GMRES ones. We focus on the different DD preconditioners, since, up to our knowledge, this is the first attempt to apply these techniques over the FPSI problems coupling.

We will introduce the Robin-Robin method because the other algorithms are just particular cases. The transmission conditions for the Navier-Stokes/Biot problem are (4a)-(4d): (4a) is a Dirichlet boundary condition and (4b)-(4c) are Neumann boundary conditions. (4d) is a Robin boundary condition. The idea is to use linear combinations of these transmission conditions, in order to get a set of Robin boundary conditions, as it has been done for FSI in [5, 6]. Let us start with the Robin boundary conditions that we will use for the fluid subproblem. For the normal component, we add the Dirichlet

boundary condition (4a) times α_f and the normal component of the Neumann boundary condition (4c), where α_f is the combination parameter. For the tangential component, there is no Dirichlet boundary condition for the fluid subproblem. Instead, we have the Robin condition (4d). Thus, we add (4d) times α_f and the tangential component of (4c). We supplement the fluid subproblem with the following transmission condition:

$$\alpha_f \boldsymbol{u}_f^{n+1} \cdot \boldsymbol{n} + \boldsymbol{n} \cdot (\boldsymbol{\sigma}_f^{n+1} \cdot \boldsymbol{n}) = \alpha_f (\boldsymbol{u}_s^{n+1} + \boldsymbol{q}^{n+1}) \cdot \boldsymbol{n} + \boldsymbol{n} \cdot (\boldsymbol{\sigma}_s^{n+1} \cdot \boldsymbol{n}), \quad (43a)$$

$$\alpha_f \boldsymbol{u}_f^{n+1} \cdot \boldsymbol{t} + \left(1 + \alpha_f \frac{\sqrt{\kappa}}{\gamma}\right) \boldsymbol{t} \cdot (\boldsymbol{\sigma}_f^{n+1} \cdot \boldsymbol{n}) = \alpha_f \boldsymbol{u}_s^{n+1} \cdot \boldsymbol{t} + \boldsymbol{t} \cdot (\boldsymbol{\sigma}_s^{n+1} \cdot \boldsymbol{n}), \quad (43b)$$

Similarly, for the structure problem, we combine (4a)-(4d). First, we consider (4a) by α_s minus (4b) and the normal component of (4c), respectively. The second transmission condition is obtained combining linearly (44b) and (4d) to the tangential component of (4c). We supplement the poroelastic structure with the transmission conditions:

$$\alpha_s (\boldsymbol{u}_s^{n+1} + \boldsymbol{q}^{n+1}) \cdot \boldsymbol{n} - \boldsymbol{n} \cdot (\boldsymbol{\sigma}_s^{n+1} \cdot \boldsymbol{n}) = \alpha_s \boldsymbol{u}_f^{n+1} \cdot \boldsymbol{n} - \boldsymbol{n} \cdot (\boldsymbol{\sigma}_f^{n+1} \cdot \boldsymbol{n}), \quad (44a)$$

$$\alpha_s \boldsymbol{u}_s^{n+1} \cdot \boldsymbol{t} - \boldsymbol{t} \cdot (\boldsymbol{\sigma}_s^{n+1} \cdot \boldsymbol{n}) = \alpha_s \boldsymbol{u}_f^{n+1} \cdot \boldsymbol{t} + \left(\alpha_s \frac{\sqrt{\kappa}}{\gamma} - 1\right) \boldsymbol{t} \cdot (\boldsymbol{\sigma}_f^{n+1} \cdot \boldsymbol{n}), \quad (44b)$$

$$\alpha_s (\boldsymbol{q}^{n+1} + \boldsymbol{u}_s^{n+1}) \cdot \boldsymbol{n} + p_p^{n+1} = \alpha_s \boldsymbol{u}_f^{n+1} \cdot \boldsymbol{n} - \boldsymbol{n} \cdot (\boldsymbol{\sigma}_f^{n+1} \cdot \boldsymbol{n}). \quad (44c)$$

The combination parameters must satisfy $\alpha_f \neq -\alpha_s$. Furthermore, we assume $\alpha_f, \alpha_s > 0$ in order for the problem to be well posed. Robin interface conditions motivate new partitioned procedures, some of which feature better convergence than the DN method. Notice that the classical DN and ND algorithms can be recovered with particular values of the combination parameters ($\alpha_f = \infty$, $\alpha_s = 0$ for the former, and $\alpha_f = 0$, $\alpha_s = \infty$ for the latter). Other particular cases, studied in [5], are the Neumann-Robin ($\alpha_f = 0$), Robin-Neumann ($\alpha_s = 0$), Dirichlet-Robin ($\alpha_f = \infty$), and Robin-Dirichlet ($\alpha_s = \infty$) schemes.

Let us state the Robin-Robin algorithm with Richardson iterations, linearized with a fixed point method. We consider the time step value t^{n+1} and the discrete problem in time. In space, we use the strong form of the problem, since the discretization in space does not introduce any interesting issue. We also omit the time index $n+1$ for the sake of simplicity. The iteration $k+1$ of this algorithm consists of:

Robin-Robin algorithm
Given $\boldsymbol{\eta}^n$, $\boldsymbol{\eta}^{n-1}$, $\boldsymbol{u}^n$ and the value at the previous iteration $\boldsymbol{\eta}^k$, find $\boldsymbol{u}_s^{k+1}$, $\boldsymbol{u}_f^{k+1}$ p_f^{k+1} and p_p^{k+1} such that,

1. Fluid problem (Robin boundary condition)

$$\rho_f \delta_t \boldsymbol{u}_f^{k+1} + \rho_f (\boldsymbol{u}_f^* - \boldsymbol{w}^*) \cdot \nabla \boldsymbol{u}_f^{k+1} - \nabla \cdot \boldsymbol{\sigma}_f^{k+1} = \boldsymbol{f}_f \qquad \text{in } \Omega_*^f, \quad (45a)$$

$$\nabla \cdot \boldsymbol{u}_f^{k+1} = 0 \qquad \text{in } \Omega_*^f, \quad (45b)$$

supplemented with

$$\alpha_f \boldsymbol{u}_f^{k+1} \cdot \boldsymbol{n} + \boldsymbol{n} \cdot (\boldsymbol{\sigma}_f^{k+1} \cdot \boldsymbol{n}) = \alpha_f (\boldsymbol{u}_s^k + \boldsymbol{q}^k) \cdot \boldsymbol{n} + \boldsymbol{n} \cdot (\boldsymbol{\sigma}_s^k \cdot \boldsymbol{n}), \quad (45c)$$

$$\alpha_f \boldsymbol{u}_f^{k+1} \cdot \boldsymbol{t} + \left(1 + \alpha_f \frac{\sqrt{\kappa}}{\gamma}\right) \boldsymbol{t} \cdot (\boldsymbol{\sigma}_f^{k+1} \cdot \boldsymbol{n}) = \alpha_f \boldsymbol{u}_s^k \cdot \boldsymbol{t} + \boldsymbol{t} \cdot (\boldsymbol{\sigma}_s^k \cdot \boldsymbol{n}), \quad (45d)$$

2. Structure problem (Robin boundary condition)

$$\rho_p \mathrm{d}_t \boldsymbol{u}_s^{k+1} + \rho_d \mathrm{d}_t \boldsymbol{q}^{k+1} - \nabla \cdot \boldsymbol{\sigma}_s^{\mathrm{dev}}(\boldsymbol{\eta}^{k+1}) + \nabla p_p^{k+1} = \boldsymbol{f}_s \qquad \text{in } \Omega_*^p, \tag{46a}$$

$$\rho_d \mathrm{d}_t \boldsymbol{u}_s^{k+1} + \rho_d \mathrm{d}_t \frac{\boldsymbol{q}^{k+1}}{\phi} + \kappa^{-1} \boldsymbol{q}^{k+1} + \nabla p_p^{k+1} = \boldsymbol{f}_d \qquad \text{in in } \Omega_*^p, \tag{46b}$$

$$\nabla \cdot (\boldsymbol{u}_s^{k+1} + \boldsymbol{q}^{k+1}) = 0 \qquad \text{in in } \Omega_*^p. \tag{46c}$$

supplemented with

$$\alpha_s(\boldsymbol{u}_s^{k+1} + \boldsymbol{q}^{k+1}) \cdot \boldsymbol{n} - \boldsymbol{n} \cdot (\boldsymbol{\sigma}_s^{k+1} \cdot \boldsymbol{n}) = \alpha_s \boldsymbol{u}_f^{k+1} \cdot \boldsymbol{n} - \boldsymbol{n} \cdot (\boldsymbol{\sigma}_f^{n+1} \cdot \boldsymbol{n}), \tag{47}$$

$$\alpha_s \boldsymbol{u}_s^{k+1} \cdot \boldsymbol{t} - \boldsymbol{t} \cdot (\boldsymbol{\sigma}_s^{k+1} \cdot \boldsymbol{n}) = \alpha_s \boldsymbol{u}_f^{k+1} \cdot \boldsymbol{t} + \left(\alpha_s \frac{\sqrt{\kappa}}{\gamma} - 1 \right) \boldsymbol{t} \cdot (\boldsymbol{\sigma}_f^{k+1} \cdot \boldsymbol{n}), \tag{48}$$

$$\alpha_s(\boldsymbol{q}^{k+1} + \boldsymbol{u}_s^{k+1}) \cdot \boldsymbol{n} + p_p^{k+1} = \alpha_s \boldsymbol{u}_f^{k+1} \cdot \boldsymbol{n} - \boldsymbol{n} \cdot (\boldsymbol{\sigma}_f^{k+1} \cdot \boldsymbol{n}). \tag{49}$$

The convective velocity is linearized around u^* and the fluid domain, solid domain and mesh velocity around Ω_*^f and Ω_*^s.

Remark 7.1 *If we choose $\alpha_f = \infty$, $\alpha_s = 0$ in (43) and (44), we do not recover a Dirichlet-Neumann algorithm, strictly speaking. In fact, while a Dirichlet condition is imposed on the normal component of the velocity, a Robin condition is imposed on the tangential one. However, the structure problem is endowed with a Neumann interface condition. In the same way, if we set $\alpha_f = 0$, $\alpha_s = \infty$, the resulting method is not properly a Neumann-Dirichlet one. Nevertheless, we will address to those schemes as DN and ND ones.*

The main issue in using Robin transmission conditions is the evaluation of appropriate combination parameters α_f and/or α_s capable of improving the convergence properties of the classical DN method. Robin-Robin methods have been adopted for other applications (see, e.g., [33] for the Stokes-Darcy coupling) and they proved to be successful only for the right choices of the combination parameters. In [5], effective values are provided by simplified models for the fluid and the structure. For the fluid-poroelastic structure interaction, we employ the same simplified fluid model to derive α_s. On the other hand, a new simplified structure model needs to be studied to get a suitable value for α_f.

In the following, we restrict our attention to the Dirichlet-Neumann, Robin-Neumann (RN), and Robin-Robin (RR) algorithms. We expect the RN method to be the best one. The RN algorithm was the optimal choice in [5, 6].

7.1. A simplified fluid-structure model

In order to analyze the convergence properties of the DN, RR, and RN algorithms for the FPSI problem, we introduce a simplified fluid-structure model.

We take a rectangular fluid domain $\Omega^f \subset \mathbb{R}^2$ of height R and length L. The structure domain $\Omega^p \subset \mathbb{R}^2$ is a rectangle of length L and height h_s, placed on the upper side of Ω^f.The deformation of the structure is assumed to be very small so that the fluid domain can be considered fixed.

In Ω^f we consider a potential fluid flow:

$$\rho_f \partial_t \boldsymbol{u}_f + \nabla p_f = \mathbf{0} \qquad \text{in } \Omega^f \times (0,T), \tag{50a}$$
$$\nabla \cdot \boldsymbol{u}_f = 0 \qquad \text{in } \Omega^f \times (0,T), \tag{50b}$$
$$u_f = \partial_t \eta + q \qquad \text{on } \Sigma \times (0,T), \tag{50c}$$
$$p_f = \overline{p}_f \qquad \text{on } \Gamma^f_{in} \cup \Gamma^f_{out}, \tag{50d}$$
$$u_f = 0 \qquad \text{on } \Gamma^f_{down}, \tag{50e}$$

with suitable initial conditions. The non-bold variable refers to the normal component of the associated vector, e.g. $q = \boldsymbol{q} \cdot \boldsymbol{n}$. Thanks to the definition of the added-mass operator $\mathcal{M}$ (see, e.g., [20]), we have

$$p_f = \hat{p}_f - \rho_f \mathcal{M}(\partial_{tt}\eta + \mathrm{D}_t q), \tag{51}$$

where $\hat{p}_f$ accounts for possible non-homogeneous boundary conditions on $\partial\Omega^f \backslash \Sigma$.

For the structure subproblem, we deal with the limit case described in Section 4.2. Small displacements are assumed and ∂_t and D_t coincide. Moreover, we neglect the term $\nabla \cdot \boldsymbol{\sigma}_s^{\mathrm{dev}}(\boldsymbol{\eta})$ in the structure momentum balance equation, i.e. we assume negligible shear deformations. Hence, the structure model written in terms of displacement $\boldsymbol{\eta}$ (instead of velocity $\boldsymbol{u}_s$) is governed by equations

$$\rho_p \partial_{tt}\boldsymbol{\eta} + a\boldsymbol{\eta} + \nabla p_p = \mathbf{0} \qquad \text{in } \Omega^p \times (0,T), \tag{52a}$$
$$\rho_d \partial_{tt}\boldsymbol{\eta} + \kappa^{-1}\boldsymbol{q} + \nabla p_p = \mathbf{0} \qquad \text{in } \Omega^p \times (0,T), \tag{52b}$$
$$\nabla \cdot \boldsymbol{\eta} = 0 \qquad \text{in } \Omega^p \times (0,T), \tag{52c}$$
$$p_p = p_f \qquad \text{on } \Sigma \times (0,T), \tag{52d}$$
$$p_p = 0 \qquad \text{on } \Gamma^p_{in} \cup \Gamma^p_{out} \cup \Gamma^p_{up}, \tag{52e}$$

where $a = E/(1-\nu^2)R^2$, E being the Young modulus and ν the Poisson ratio of the matrix. The reaction term in (52a) represents the transversal membrane effects appearing when the structure equations are written in axisymmetric form. Problem (52) must be supplemented with initial conditions. Moreover, drained conditions (52e) have been imposed on $\partial\Omega^p \backslash \Sigma$.

Equation (52a) for the normal component η can be written as

$$\rho_p \partial_{tt}\eta + a\eta + \frac{\partial p_p}{\partial \boldsymbol{n}}\Big|_\Sigma = 0. \tag{53}$$

By taking the divergence of (52a) and exploiting (52c), system (52) may be reformulated as follows

$$-\triangle p_p = 0 \qquad \text{in } \Omega^p, \tag{54a}$$
$$p_p = p_f \qquad \text{on } \Sigma, \tag{54b}$$
$$p_p = 0 \qquad \text{on } \Gamma^p_{in} \cup \Gamma^p_{out} \cup \Gamma^p_{up}. \tag{54c}$$

For any $p_f \in H^{1/2}(\Sigma)$, equations (54) compute a pressure $p_p \in H^1(\Omega^p)$. Then, $\boldsymbol{\eta}$ and $\boldsymbol{q}$ are recovered by (52a) and (52b), respectively. Let us define the operator $\mathcal{M}_p^{-1} : H^{1/2}(\Sigma) \to H^{-1/2}(\Sigma)$ by

$$\mathcal{M}_p^{-1} p_f = -\frac{\partial p_p}{\partial \boldsymbol{n}}\Big|_\Sigma. \tag{55}$$

The Dirichlet-to-Neumann map $\mathcal{M}_p^{-1}$ can be seen as a sort of inverse added-mass operator for the structure. By plugging (51) into (55), we obtain

$$\frac{\partial p_p}{\partial \boldsymbol{n}}\Big|_\Sigma = \rho_f \mathcal{D}\partial_{tt}\eta + \rho_f \mathcal{D}\partial_t q - \mathcal{M}_p^{-1}\hat{p}_f,$$

where we called $\mathcal{D} : H^{-1/2}(\Sigma) \to H^{-1/2}(\Sigma)$ the operator deriving from the composition of $\mathcal{M}$ with $\mathcal{M}_p^{-1}$, i.e. $\mathcal{D}(\cdot) = \mathcal{M}_p^{-1}(\mathcal{M}(\cdot))$. Using this result in (53), we find that the FPSI model problem (50)-(52) is equivalent to: find η and q such that

$$(\rho_p \mathcal{I} + \rho_f \mathcal{D})\partial_{tt}\eta + a\eta + \rho_f \mathcal{D}\partial_t q = \mathcal{M}_p^{-1}\hat{p}_f, \tag{56a}$$

$$(\rho_d \mathcal{I} + \rho_f \mathcal{D})\partial_{tt}\eta + \kappa^{-1} q + \rho_f \mathcal{D}\partial_t q = \mathcal{M}_p^{-1}\hat{p}_f. \tag{56b}$$

Remark 7.2 *Equation (56a) looks like structure equation (53) with an extra operator in front of the second order time derivative and a term in $\partial_t q$. When a fluid interacts with a poroelastic structure, it acts like an "added-mass" on the structure, as in the interaction with a purely elastic structure. Moreover, an additional inertial term related to the filtration velocity appears in the structure equation.*

For the subsequent mathematical analysis, it is important to estimate the maximum eigenvalue of operator $\mathcal{D}$, denoted by $\mu_{max}^{\mathcal{D}}$. Note that, like the maximum eigenvalue of $\mathcal{M}$ $\mu_{max}^{\mathcal{M}}$ (see [20]), it is a purely geometric quantity. When dealing with a generic geometry, a closed expression for $\mu_{max}^{\mathcal{D}}$ cannot be found, but in the case of the simple geometry under consideration it is possible.

We consider the following reformulation of fluid problem (50)

$$\begin{aligned}
&-\triangle p_f = 0 && \text{in } \Omega^f \\
&\partial_y p_f = g && \text{on } \Sigma, \\
&p_f = 0 && \text{on } \Gamma_{in}^f \cup \Gamma_{out}^f, \\
&\partial_y p_f = 0 && \text{on } \Gamma_{down}^f.
\end{aligned}$$

coupled to the model structure problem (54). By expressing function g as

$$g(x) = \sum_{k\geq 1} g_k \sin\Big(k\pi\frac{x}{L}\Big),$$

we compute the fluid pressure $p_f(x,y)$ (see [20]) and extract its value at the interface $y = R$

$$p_f(x)|_\Sigma = \mathcal{M}g = \sum_{k\geq 1} g_k \frac{L}{k\pi}\frac{\cosh\left(k\pi\frac{R}{L}\right)}{\sinh\left(k\pi\frac{R}{L}\right)}\sin\Big(k\pi\frac{x}{L}\Big) = \sum_{k\geq 1} p_{f,k}.$$

Plugging this function in (54b) allows us to compute the pressure $p_p(x,y)$ in the poroelastic medium

$$p_p(x,y) = \sum_{k\geq 1} g_k \frac{L}{k\pi}\frac{\cosh\left(k\pi\frac{R}{L}\right)}{\sinh\left(k\pi\frac{R}{L}\right)}\frac{1}{\sinh\left(k\pi\frac{h_s}{L}\right)}\sin\Big(k\pi\frac{x}{L}\Big)\sinh\left(k\pi\frac{R+h_s-y}{L}\right).$$

Then, since $\boldsymbol{n}$ indicates the y direction, we can write

$$\begin{aligned}
\mathcal{D}g = -\frac{\partial p_p}{\partial \boldsymbol{n}}\Big|_\Sigma &= \sum_{k\geq 1} g_k \frac{\cosh\left(k\pi\frac{R}{L}\right)}{\sinh\left(k\pi\frac{R}{L}\right)}\frac{\cosh\left(k\pi\frac{h_s}{L}\right)}{\sinh\left(k\pi\frac{h_s}{L}\right)}\sin\Big(k\pi\frac{x}{L}\Big) \\
&= \sum_{k\geq 1} p_{f,k}\frac{k\pi}{L}\frac{1}{\tanh\left(k\pi\frac{h_s}{L}\right)}.
\end{aligned} \tag{57}$$

Finding the eigenvalues $\mu_k^{\mathcal{D}}$, $k = 1, 2, ...,$ of $\mathcal{D}$ associated to the eigenvector $g = g_k \sin(k\pi\frac{x}{L})$ means to solve the eigenvalue problem

$$\mathcal{D}g = \mu_k^{\mathcal{D}} g,$$

which implies

$$\mu_k^{\mathcal{D}} = \frac{1}{\tanh\left(k\pi\frac{R}{L}\right)\tanh\left(k\pi\frac{h_s}{L}\right)}.$$

Thus, the maximum eigenvalue is for $k = 1$

$$\mu_{max}^{\mathcal{D}} = \frac{1}{\tanh\left(\pi\frac{R}{L}\right)\tanh\left(\pi\frac{h_s}{L}\right)}.$$

Figures 2(a) and 2(b) show the value of $\mu_{max}^{\mathcal{D}}$ varying the fluid and the structure geometry, i.e. L and R, and L and h_s, respectively.

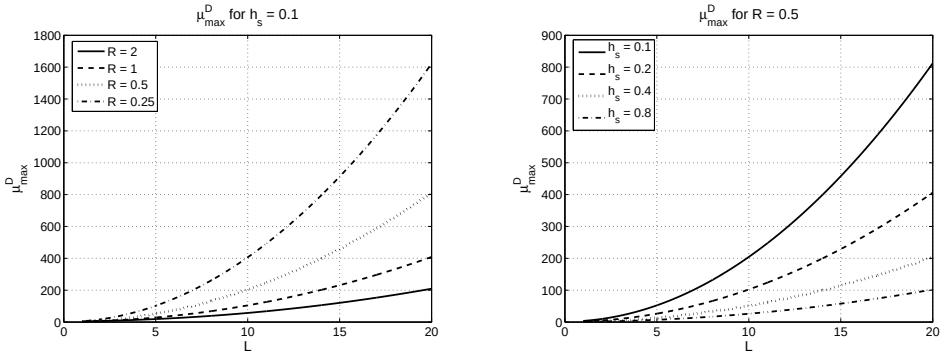

(a) varying L and R

(b) varying L and h_s

Figure 2: Largest eigenvalue of operator $\mathcal{D}$ as a function of (a) fluid domain length L and height H and (b) structure domain length L and thickness h_s.

7.2. The Dirichlet-Neumann algorithm

In this subsection, we aim at analyzing the convergence properties of the DN method applied to the simplified FPSI problem (50)-(52).

We discretize in time problem (50)-(52) with the BDF1 scheme for both fluid and structure equations. The Dirichlet-Neumann algorithm supplemented with a relaxation technique reads: at time step t^{n+1} and iteration $k+1$, with $n, k > 0$, given $\boldsymbol{u}_f^n$, $\boldsymbol{\eta}^n$, and $\boldsymbol{\eta}^{n-1}$, solve

(i) Fluid problem (Dirichlet boundary condition): Find $\boldsymbol{u}_f^{k+1}$, p_f^{k+1} such that

$$\rho_f \delta_t \boldsymbol{u}_f^{k+1} + \nabla p_f^{k+1} = \boldsymbol{0} \qquad \text{in } \Omega^f, \tag{58a}$$

$$\nabla \cdot \boldsymbol{u}_f^{k+1} = 0 \qquad \text{in } \Omega^f, \tag{58b}$$

$$u_f^{k+1} = \delta_t \eta^k + q^k \qquad \text{on } \Sigma, \tag{58c}$$

$$p_f^{k+1} = \overline{p}_f \qquad \text{on } \Gamma_{in}^f \cup \Gamma_{out}^f, \tag{58d}$$

$$u_f^{k+1} = 0 \qquad \text{on } \Gamma_{down}^f. \tag{58e}$$

(ii) Structure problem (Neumann boundary condition): Find $\widetilde{\boldsymbol{\eta}}^{k+1}$, $\widetilde{\boldsymbol{q}}^{k+1}$, p_p^{k+1} such that

$$\rho_p \delta_{tt} \widetilde{\boldsymbol{\eta}}^{k+1} + a\widetilde{\boldsymbol{\eta}}^{k+1} + \nabla p_p^{k+1} = \mathbf{0} \qquad \text{in } \Omega^p, \tag{59a}$$

$$\rho_d \delta_{tt} \widetilde{\boldsymbol{\eta}}^{k+1} + \kappa^{-1}\widetilde{\boldsymbol{q}}^{k+1} + \nabla p_p^{k+1} = \mathbf{0} \qquad \text{in } \Omega^p, \tag{59b}$$

$$\nabla \cdot \widetilde{\boldsymbol{\eta}}^{k+1} = 0 \qquad \text{in } \Omega^p, \tag{59c}$$

$$p_p^{k+1} = p_f^{k+1} \qquad \text{on } \Sigma, \tag{59d}$$

$$p_p^{k+1} = 0 \qquad \text{on } \Gamma_{in}^p \cup \Gamma_{out}^p \cup \Gamma_{up}^p. \tag{59e}$$

(iii) Relaxation step

$$\eta^{k+1} = \omega\widetilde{\eta}^{k+1} + (1-\omega)\eta^k, \tag{60a}$$

$$q^{k+1} = \omega\widetilde{q}^{k+1} + (1-\omega)q^k. \tag{60b}$$

(iv) Convergence test: if the stopping criterion is satisfied, then set $\boldsymbol{u}_f^{n+1} = \boldsymbol{u}_f^{k+1}$, $p_f^{n+1} = p_f^{k+1}$, $\boldsymbol{\eta}^{n+1} = \boldsymbol{\eta}^{k+1}$, $\boldsymbol{q}^{n+1} = \boldsymbol{q}^{k+1}$, and $p_p^{n+1} = p_p^{k+1}$.

The relaxation parameter might be necessary to guarantee the convergence of the method.

Theorem 7.1 *The Dirichlet-Neumann iterative method applied to the solution of the FPSI test problem (50)-(52) converges to the "monolithic" solution provided the following condition on the relaxation parameter is satisfied*

$$0 < \omega \leq \frac{2(\rho_p + a\delta t^2)}{(\rho_p + a\delta t^2 + 2\rho_f \mu_{max}^{\mathcal{D}})}. \tag{61}$$

Proof. Let us introduce the normal component of the structure velocity $\widetilde{u}_s^{k+1} = (\widetilde{\eta}^{k+1} - \eta^n)/\delta t$. The DN algorithm (58)-(59) is equivalent to: find $\widetilde{u}_s^{k+1}$ and $\widetilde{q}^{k+1}$

$$\begin{aligned}
&\frac{\rho_p}{\delta t}\left(\widetilde{u}_s^{k+1} - u_s^n\right) + a\delta t\widetilde{u}_s^{k+1} + \frac{\rho_f}{\delta t}\mathcal{D}\left(q^k - q^n + u_s^k - u_s^n\right) = \mathcal{M}_p^{-1}\hat{p}_f^{n+1} - a\eta^n,\\
&\frac{\rho_d}{\delta t}\left(\widetilde{u}_s^{k+1} - u_s^n\right) + \kappa^{-1}\widetilde{q}^{k+1} + \frac{\rho_f}{\delta t}\mathcal{D}\left(q^k - q^n + u_s^k - u_s^n\right) = \mathcal{M}_p^{-1}\hat{p}_f^{n+1}.
\end{aligned} \tag{62}$$

From relaxation step (60), it follows that

$$\widetilde{u}_s^{k+1} = \frac{1}{\omega}u_s^{k+1} - \frac{1-\omega}{\omega}u_s^k, \quad \text{and} \quad \widetilde{q}^{k+1} = \frac{1}{\omega}q^{k+1} - \frac{1-\omega}{\omega}q^k.$$

Then, the previous system is equivalent to

$$\begin{aligned}
&\frac{1}{\omega}\left[\left(\frac{\rho_p}{\delta t} + a\delta t\right)\mathcal{I}\right]u_s^{k+1} - \left[\frac{1-\omega}{\omega}\left(\frac{\rho_p}{\delta t} + a\delta t\right)\mathcal{I} - \frac{\rho_f}{\delta t}\mathcal{D}\right]u_s^k + \frac{\rho_f}{\delta t}\mathcal{D}q^k = f(u_s^n, q^n, \hat{p}_f^{n+1}),\\
&\frac{1}{\omega}\frac{\rho_d}{\delta t}u_s^{k+1} + \frac{\kappa^{-1}}{\omega}q^{k+1} - \left[\frac{1-\omega}{\omega}\frac{\rho_d}{\delta t}\mathcal{I} - \frac{\rho_f}{\delta t}\mathcal{D}\right]u_s^k - \left[\frac{1-\omega}{\omega}\kappa^{-1}\mathcal{I} - \frac{\rho_f}{\delta t}\mathcal{D}\right]q^k = g(u_s^n, q^n, \hat{p}_f^{n+1}),
\end{aligned}$$

for suitable functions f and g. In turn, this corresponds to iterative method

$$u_s^{k+1} = \left[(1-\omega)\mathcal{I} - \omega\frac{\rho_f}{\rho_p + a\delta t^2}\mathcal{D}\right]u_s^k - \omega\frac{\rho_f}{\rho_p + a\delta t^2}\mathcal{D}q^k + \tilde{f}(u_s^n, q^n, \hat{p}_f^{n+1}), \tag{63a}$$

$$\begin{aligned}
q^{k+1} =& \omega\kappa\left(\frac{\rho_d}{\rho_p + a\delta t^2} - 1\right)\frac{\rho_f}{\delta t}\mathcal{D}u_s^k + \left[(1-\omega)\mathcal{I} + \omega\kappa\left(\frac{\rho_d}{\rho_p + a\delta t^2} - 1\right)\frac{\rho_f}{\delta t}\mathcal{D}\right]q^k\\
&+ \tilde{g}(u_s^n, q^n, \hat{p}_f^{n+1}),
\end{aligned} \tag{63b}$$

for suitable functions $\tilde{f}$ and $\tilde{g}$.

The solution of the DN method coincides with the fixed point of the iterative method (63). Sufficient conditions for the convergence of that fixed point method are

$$\left|(1-\omega) - \omega\frac{\rho_f \mu_i^{\mathcal{D}}}{\rho_p + a\delta t^2}\right| + \left|\omega\frac{\rho_f \mu_i^{\mathcal{D}}}{\rho_p + a\delta t^2}\right| < 1,$$

$$\left|\omega\kappa\left(\frac{\rho_d}{\rho_p + a\delta t^2} - 1\right)\frac{\rho_f}{\delta t}\mu_i^{\mathcal{D}}\right| + \left|(1-\omega) + \omega\kappa\left(\frac{\rho_d}{\rho_p + a\delta t^2} - 1\right)\frac{\rho_f}{\delta t}\mu_i^{\mathcal{D}}\right| < 1,$$

which lead to

$$0 < \omega \leq \frac{2(\rho_p + a\delta t^2)}{(\rho_p + a\delta t^2 + 2\rho_f \mu_{max}^{\mathcal{D}})}, \tag{64a}$$

$$0 < \omega \leq \frac{2}{1 + 2\kappa\frac{\rho_f}{\delta t}\left(1 - \frac{\rho_d}{\rho_p + a\delta t^2}\right)\mu_{max}^{\mathcal{D}}}. \tag{64b}$$

For the values of κ which allow us to derive model problem (52), condition (64b) is far less restrictive than condition (64a). Thus, the convergence of the DN algorithm (58)-(59)-(60) depends only on the latter. Numerical experiments reported in Section 8.3 confirm this result. □

7.3. The Robin-Robin and the Robin-Neumann algorithms

The Robin-Robin algorithm for the time discrete version of problem (50)-(52) reads: at time step t^{n+1} and iteration $k+1$, with $n, k > 0$, given $\boldsymbol{u}_f^n$, $\boldsymbol{\eta}^n$, and $\boldsymbol{\eta}^{n-1}$, solve

(i) Fluid problem (Robin boundary condition): Find $\boldsymbol{u}_f^{k+1}$, p_f^{k+1} as in (58) but replacing interface condition (58c) with

$$\alpha_f u_f^{k+1} - p_f^{k+1} = \alpha_f(\delta_t \eta^k + q^k) - p_p^k \quad \text{on } \Sigma. \tag{65}$$

(ii) Structure problem (Robin boundary condition): Find $\widetilde{\boldsymbol{\eta}}^{k+1}$, $\widetilde{\boldsymbol{q}}^{k+1}$, p_p^{k+1} as in (59) but replacing interface condition (59d) with

$$\alpha_s(u_s^{k+1} + q^{k+1}) + p_p^{k+1} = \alpha_s u_f^{k+1} + p_f^{k+1} \quad \text{on } \Sigma.$$

Steps (iii) and (iv) are common to the DN algorithm.

As already highlighted, a central role in the convergence of the Robin-Robin algorithm is played by the combination parameters α_f and α_s. We adopt the α_s computed in [5], i.e.

$$\alpha_s = \frac{\rho_f}{\delta t}\mu_{max}^{\mathcal{M}}, \tag{66}$$

where $\mu_{max}^{\mathcal{M}}$ is the largest eigenvalue of the added-mass operator (see [20]). To derive a possible value for α_f, we consider simplified model (53). We consider the normal component of equations (52a)-(52b), discretize them in time with the BDF1 scheme and plug (57) into them to get

$$\rho_p \delta_t u_s^{n+1} + a\delta t u_s^{n+1} - \sum_{k\geq 1} p_{f,k}^{n+1}\frac{k\pi}{L}\frac{1}{\tanh\left(k\pi\frac{h_s}{L}\right)} = -a\eta^n, \tag{67a}$$

$$\rho_d \delta_t u_s^{n+1} + \kappa^{-1} q^{n+1} - \sum_{k\geq 1} p_{f,k}^{n+1}\frac{k\pi}{L}\frac{1}{\tanh\left(k\pi\frac{h_s}{L}\right)} = 0. \tag{67b}$$

If we truncate the sum at the first element, (67) becomes

$$\left(\frac{\rho_p}{\delta t}+a\delta t\right)u_s^{n+1}=\left(\frac{\pi}{L}\frac{1}{\tanh\left(\pi\frac{h_s}{L}\right)}\right)p_{f,1}^{n+1}+\frac{\rho_p}{\delta t}u_s^n-a\eta^n,$$
$$\frac{\rho_d}{\delta t}u_s^{n+1}+\kappa^{-1}q^{n+1}=\left(\frac{\pi}{L}\frac{1}{\tanh\left(\pi\frac{h_s}{L}\right)}\right)p_{f,1}^{n+1}+\frac{\rho_d}{\delta t}u_s^n,$$

which is equivalent to

$$u_s^{n+1}=\frac{1}{\frac{\rho_p}{\delta t}+a\delta t}\left(\frac{\pi}{L}\frac{1}{\tanh\left(\pi\frac{h_s}{L}\right)}\right)p_{f,1}^{n+1}+\frac{\rho_p}{\rho_p+a\delta t^2}u_s^n-\frac{a\delta t}{\rho_p+a\delta t^2}\eta^n, \tag{68a}$$

$$q^{n+1}=\kappa\left(1-\frac{\rho_d}{\rho_p+a\delta t^2}\right)\left(\frac{\pi}{L}\frac{1}{\tanh\left(\pi\frac{h_s}{L}\right)}\right)p_{f,1}^{n+1}+\kappa\frac{a\delta t}{\rho_p+a\delta t^2}(\delta t u_s^n+\eta^n). \tag{68b}$$

By summing (68a) to (68b) and thanks to the admissibility condition (4a), we find

$$\begin{aligned}u_f^{n+1}=&\frac{\pi}{L}\frac{1}{\tanh\left(\pi\frac{h_s}{L}\right)}\frac{1}{\rho_p+a\delta t^2}\left[\delta t+\kappa(\rho_p-\rho_d+a\delta t^2)\right]p_{f,1}^{n+1}\\&+\frac{\rho_p+\kappa a\delta t^2}{\rho_p+a\delta t^2}u_s^n-\frac{a\delta t}{\rho_p+a\delta t^2}(1-\kappa)\eta^n.\end{aligned} \tag{69}$$

If $p_{f,1}^{n+1}$ is a good approximation for p_f^{n+1}, this equation suggests the use of the following combination parameter

$$\alpha_f=\left(\rho_p+a\delta t^2\right)\frac{L}{\pi}\tanh\left(\pi\frac{h_s}{L}\right)\frac{1}{\delta t+\kappa(\rho_p-\rho_d+a\delta t^2)} \tag{70}$$

in Robin transmission condition (65). For the values of κ which allow us to derive model problem (52), α_f could be simplified in the following way

$$\alpha_f\sim\left(\frac{\rho_p}{\delta t}+a\delta t\right)\tanh\left(\pi\frac{h_s}{L}\right)\frac{L}{\pi}. \tag{71}$$

Even though (69) prescribes an interface condition only on the normal component of the velocity, we impose the Robin condition with the same α_f also for the tangential component. Moreover, the same value of α_f can be used even for more general structure models, whose behavior is similar to the one predicted by (53).

The Robin-Neumann algorithm is recovered from the Robin-Robin method by choosing α_f as in (70) and $\alpha_s=0$. In the classical FSI problems, the RN algorithm proves to be the best in terms of convergence properties, see [5, 6]. For this reason, we check its performance when applied to FPSI problems.

The following theorem states the convergence properties of the RN algorithm.

Theorem 7.2 *The Robin-Neumann iterative method applied to the solution of the FPSI test problem (50)-(52) converges to the "monolithic" solution provided the following condition on the relaxation parameter is satisfied*

$$0<\omega\leq 2. \tag{72}$$

Proof. By discretizing in time (51) with the BDF1 scheme and using the admissibility constraint, we know that

$$u_f^{k+1}=-\frac{\delta t}{\rho_f}\mathcal{M}^{-1}p_f^{k+1}+u_f^n+\frac{\delta t}{\rho_f}\mathcal{M}^{-1}\hat{p}_f.$$

If we approximate p_f^{k+1} in this inequality with $p_{f,1}^{k+1}$ and invoke it in (69), we get

$$\left(\alpha_f \frac{\delta t}{\rho_f}\mathcal{M}^{-1} + 1\right) p_{f,1}^{k+1} = f(u_s^n, u_f^n, \eta^n), \tag{73}$$

where α_f is defined by (70) and f is a suitable function. Combining (73) to the fixed point method associated to (68)

$$\widetilde{u}_s^{k+1} = \frac{1}{\frac{\rho_p}{\delta t} + a\delta t}\left(\frac{\pi}{L}\frac{1}{\tanh\left(\pi\frac{h_s}{L}\right)}\right) p_{f,1}^{k+1} + \frac{\rho_p}{\rho_p + a\delta t^2}u_s^n - \frac{a\delta t}{\rho_p + a\delta t^2}\eta^n,$$
$$\widetilde{q}^{k+1} = \kappa\left(1 - \frac{\rho_d}{\rho_p + a\delta t^2}\right)\left(\frac{\pi}{L}\frac{1}{\tanh\left(\pi\frac{h_s}{L}\right)}\right) p_{f,1}^{k+1} + \kappa\frac{a\delta t}{\rho_p + a\delta t^2}(\delta t u_s^n + \eta^n),$$

we obtain

$$\widetilde{u}_s^{k+1} = g(u_s^n, u_f^n, \eta^n),$$
$$\widetilde{q}^{k+1} = h(u_s^n, u_f^n, \eta^n),$$

for suitable functions g and h. A sufficient condition for the convergence of such a fixed point method is

$$|1 - \omega| < 1, \tag{74}$$

from which (72) follows.

□

Remark 7.3 *The value of α_f has been calculated for the simple domain under consideration. When the geometry is more complicated (e.g. a stenotic artery) and it is impossible to find a closed expression for $\mu_{max}^{\mathcal{D}}$, the RN algorithm becomes less effective. A possible solution is to replace the Richardson iterations of the RN scheme by GMRES ones which are less sensitive to the value of α_s (see [6]).*

8. Numerical experiments

8.1. Convergence rates for Darcy and Biot problems

Let us start with the numerical experiments for the transient Darcy problem (12). In order to check the convergence rates, we propose a test problem inspired by the one used for the Darcy equations in [49]. In a square of side length one, we consider the following exact velocity solution:

$$\boldsymbol{q} = \begin{bmatrix} -2\pi\cos(2\pi x)\sin(2\pi y)t \\ -2\pi\sin(2\pi x)\cos(2\pi y)t \end{bmatrix}.$$

The pressure field is computed from equation (12a) by setting $\boldsymbol{f}_d = 0$, while g is calculated from (12b). Dirichlet boundary conditions are imposed on the four sides.

We consider linear triangular elements. The elliptic meshes employed consist of 200, 800, 3200 and 128000 elements. The element mesh parameter h is taken to be the short-edge length. The time interval under consideration is $[0, 1]$ s.

For the results in Fig. 3, we considered the OSS stabilized formulation introduced in Section 4.1 for different choices of the parameter τ_d: $\tau_d = 1,\ 0.95,\ 0.5$. The time step value we employed is $\delta t = 0.1$ s. Fig. 3 shows the L^2-norm of the velocity and pressure errors for $\phi\kappa^{-1} = 1$ and $\rho_d = 1$, at time $t = 1$ s. If $\tau_d = 1$ or the value of τ_d is close to one, the L^2-rate of convergence for the velocity is less than 2.

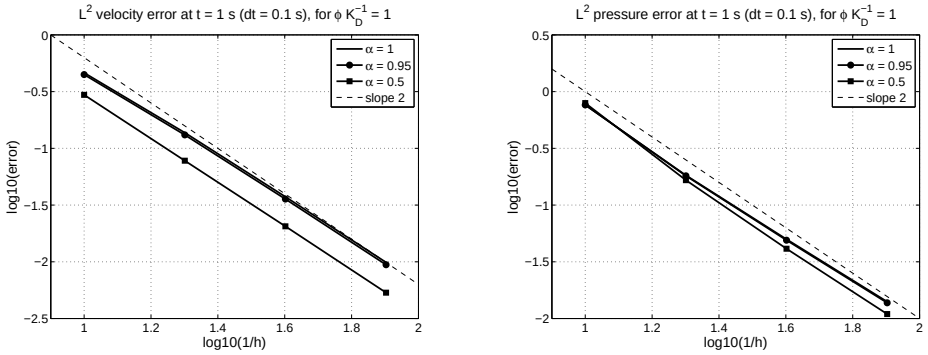

(a) velocity (b) pressure

Figure 3: Transient Darcy problem: convergence rate for the (a) velocity and (b) pressure, for $\phi\kappa^{-1} = 1$, $\rho_d = 1$.

To check the order of convergence in time, we deal with the exact velocity:

$$\boldsymbol{q} = \begin{bmatrix} -\sin(t) \\ -\sin(t) \end{bmatrix}.$$

Thus, the exact pressure solution is $p_p = \Big(\dfrac{\rho_d}{\phi}\cos(t) + \kappa^{-1}\sin(t)\Big)(x+y)$, and $g = 0$. Dirichlet boundary conditions are imposed on the four sides.

The square of size length one is discretized with an elliptic mesh of 800 triangles. Four time step values are considered ($\delta t = 0.1,\ 0.05,\ 0.025,\ 0.0125$ s) and all the errors are calculated at time $t = 1$ s. Fig. 4 shows that first order convergence in time is attained, as expected.

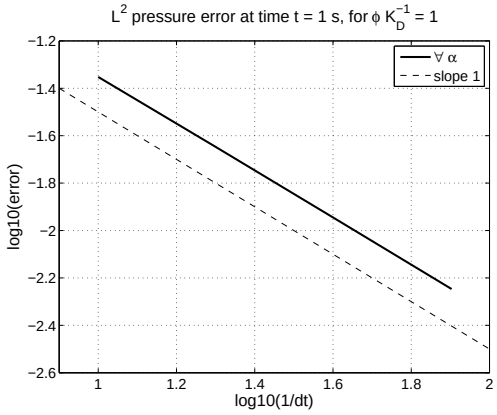

Figure 4: Transient Darcy problem: order of convergence in time for $\phi\kappa^{-1} = 1$, $\rho_d = 1$.

Finally, we perform a convergence test for the Biot system (2). The domain under consideration is again the biunit square and we impose forcing terms $\boldsymbol{f}_s$ and $\boldsymbol{f}_d$ such

that the exact solution is

$$\boldsymbol{u}_s = \begin{bmatrix} -2\pi \sin(2\pi x)\cos(2\pi y) \\ -2\pi \cos(2\pi x)\sin(2\pi y) \end{bmatrix},$$
$$\boldsymbol{q} = \phi \begin{bmatrix} -2\pi \cos(2\pi x)\sin(2\pi y)t + 2\pi \sin(2\pi x)\cos(2\pi y) \\ -2\pi \sin(2\pi x)\cos(2\pi y)t + 2\pi \cos(2\pi x)\sin(2\pi y) \end{bmatrix},$$

and

$$p = (\rho_d + \kappa^{-1}\phi t)\sin(2\pi x)\sin(2\pi y) + \kappa^{-1}\phi \cos(2\pi x)\cos(2\pi y) - \kappa^{-1}\phi.$$

We impose Dirichlet conditions on the four sides both for $\boldsymbol{u}_s$ and $\boldsymbol{q}\cdot\boldsymbol{n}$. The Dirichlet data for $\boldsymbol{u}_s$ and $\boldsymbol{q}$ are easily computed from the exact solution.

Meshes, time interval, and time step are the same ones used for the convergence test of the transient Darcy problem. Fig. 5 shows the L^2-norm of the pressure, structure and filtration velocity errors at time $t = 1$ s for $\kappa = 1$, $\rho_d = 1$, $\rho_s = 1.2$, and $\phi = 0.2$. For these results, we adopted the stabilized formulation reported in Section 4.3 and chose $\tau_d = 1, 0.5$. The same convergence rate of the Darcy and transient Darcy problem is recovered.

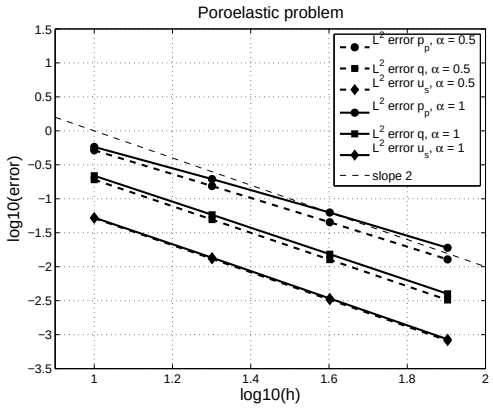

Figure 5: Biot problem: convergence rate for the pressure, structure, and filtration velocity.

When the Biot system is coupled to the Navier-Stokes equations, the stabilization method introduced in Section 4.3 works well for values of κ typical of pervious or semi-pervious media, whereas for very small values an alternative is needed. For the numerical experiments in Section 8, we used the alternative stabilization proposed in Section 4.2. It guaranteed pressure stability for the wide range of parameters we tested.

8.2. The coupled problem

We aim at analyzing how the performance of the methods described in Sections 6 and 7 are affected by the variation of the different parameters involved in FPSI problems. Our goal is again to simulate the propagation of a pressure pulse in a straight pipe with deformable porous boundaries. We consider only the $2d$ (bi-dimensional fluid and structure) approximation of this problem. We use the fluid and structure physical parameters listed in Table 1, unless otherwise specified. The other parameters of the poroelastic structure will be indicated each time, except for the slip rate coefficient γ which is always taken equal to 1.

Fluid density: $\rho_f = 1.0$ g/cm^3	Fluid viscosity: $\mu = 0.035$ poise
Structure density: $\rho_s = 1.1$ g/cm^3	Wall thickness: $h_s = 0.1$ cm
Young modulus: $E = 7 \cdot 10^5$ dyne/cm^2	Poisson coefficient: $\nu = 0.4$
Shear modulus: $G = 2.5 \cdot 10^5$ dyne/cm^2	

Table 1: Fluid and structure physical properties for the numerical tests

We impose the following Neumann condition

$$\boldsymbol{\sigma}_{f,in} = -\frac{P_{in}}{2}\Big[1 - \cos\Big(\frac{\pi t}{2.5 \cdot 10^{-3}}\Big)\Big]\mathbf{n},$$

with $P_{in} = 2 \cdot 10^4$ dyne/cm^2, at the inlet, while a homogeneous Neumann condition is imposed at the outlet.

We choose a conforming space discretization between fluid and structure: ($\mathbb{P}_1 iso \mathbb{P}_2$) - $\mathbb{P}_1$ finite elements for the fluid and stabilized $\mathbb{P}_1 - \mathbb{P}_1$ finite elements for the structure.

8.3. Comparison between the ILUT-GMRES and the DN methods

The purpose of this subsection is to compare the non-modular approach described in Section 6 and the modular DN algorithm.

We solve the FPSI problem on a structured grid of 31×11 $\mathbb{P}_1$ fluid nodes and 61×4 structure nodes. The structure mesh nodes at the interface correspond to the $\mathbb{P}_1 iso \mathbb{P}_2$ degrees of freedom for the fluid velocity. We set the structure density $\rho_s = 100$ g/cm^3 and the pores fluid density $\rho_d = 1$ g/cm^3. Notice that the effective density of the poroelastic structure is $\rho_p = \rho_s(1-\phi) + \rho_d\phi$ and the added-mass effect increases with the ratio ρ_f/ρ_p. Hence, varying the porosity makes the added-mass effect more or less critical.

We choose to adopt the explicit treatment of the nonlinearities in order to focus on the fluid-structure coupling iterations.

Let us consider first the non-modular ILUT-GMRES approach. The preconditioners adopted are the incomplete *LU* factors of the (either scaled or unscaled) monolithic system with threshold 10^{-5}. The choice of such a small value is due to the fact that it was the largest one to allow convergence in all the cases we considered, even when the diagonal scaling is not performed. Thanks to the small size of the problem, we can apply the GMRES method without restart. The tolerance used in (42) to stop the GMRES iteration is 10^{-4}.

In addition to the relative residual in (42), here denoted simply by $\boldsymbol{r}$, we define the relative residuals $\boldsymbol{r}_f$, $\boldsymbol{r}_\sigma$, and $\boldsymbol{r}_p$ as the residuals of the equations for the inner fluid, interface, and inner structure nodes, respectively. We aim at checking how all those residuals decrease with the iteration number, either with or without applying the diagonal scaling to the system matrix in (41). Figures 6 report this study for two different values of ϕ ($\phi = 0.15$ and $\phi = 0.95$) and time step ($\delta t = 2.5 \cdot 10^{-4}$ s and $\delta t = 10^{-4}$ s). The diagonal scaling allows to reduce the number of ILUT-GMRES iterations in all the cases. However, this reduction gets less important as ϕ decreases (i.e. as the added-mass effect gets less critical) and as the time step becomes small. We notice that $\boldsymbol{r}_\sigma$ is always slightly bigger than $\boldsymbol{r}_f$ and $\boldsymbol{r}_p$. The porosity being fixed, the number of iterations increases as the time step value decreases. Moreover, GMRES converges faster for small ρ_p. This confirms what found in [7]: the ILUT-GMRES algorithm shows better convergence properties for problems with large added-mass effect.

To highlight this aspect, we plot in Figure 7(a) the average number of GMRES iterations to solve monolithic system (41) for different porosities ($\phi = 0.15, 0.35, 0.55, 0.75, 0.95$), hydraulic conductivities ($\kappa \sim 10^{-6}, 10^{-8}, 10^{-10}$, 10^{-12} (cm^3 s)/g), and time step values

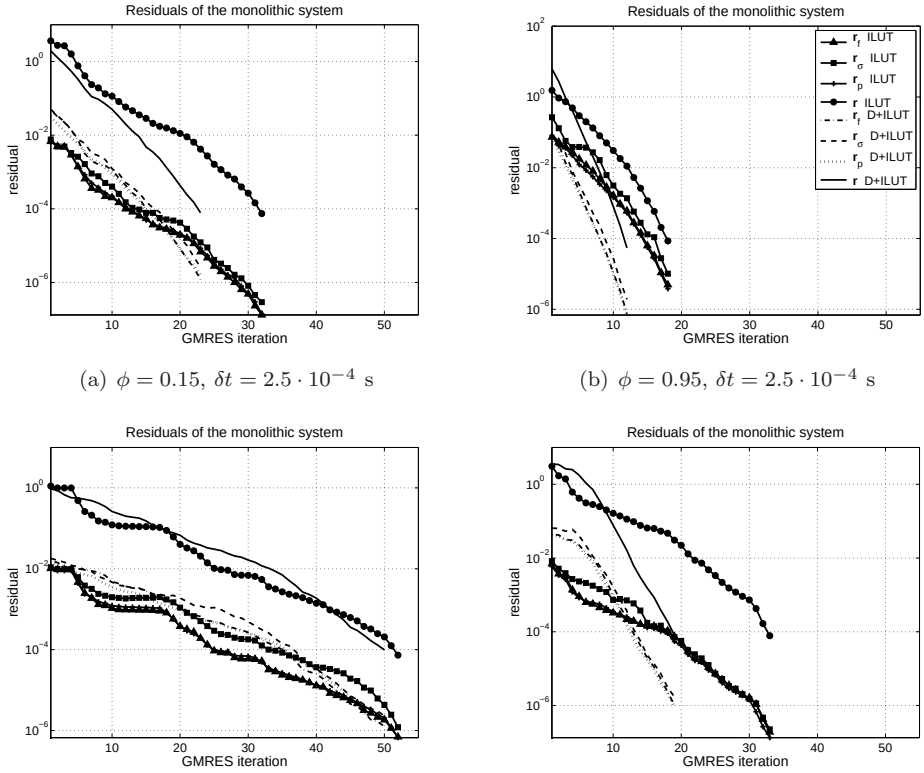

(a) $\phi = 0.15$, $\delta t = 2.5 \cdot 10^{-4}$ s

(b) $\phi = 0.95$, $\delta t = 2.5 \cdot 10^{-4}$ s

(c) $\phi = 0.15$, $\delta t = 10^{-4}$ s

(d) $\phi = 0.95$, $\delta t = 10^{-4}$ s

Figure 6: Residuals $\boldsymbol{r}$, $\boldsymbol{r}_f$, $\boldsymbol{r}_\sigma$, and $\boldsymbol{r}_p$ associated to the monolithic system, with and without scaling, for different different values of ϕ and δt. The legend in (b) is common to the four graphs.

($\delta t = 5 \cdot 10^{-4}, 2.5 \cdot 10^{-4}$ s). The larger the added-mass effect is, the fewer iterations the GMRES method requires to converge. This tendency (unaffected by the value of κ) is opposite to what happens with the DN algorithm, as Fig. 7(b) confirms. The DN method whose results are reported in Fig. 7(b) uses an Aitken relaxation procedure (see [53, 30]).

Variations in the order of magnitude of κ cause only small differences in the number of average iterations for both methods.

8.4. Comparison between the DN and the RN algorithms

In this subsection, we intend to compare two modular procedures. The first one is the DN method whose advantages and drawbacks have already been discussed in the literature. The second one is the RN algorithm which exhibits a good behavior for classical FSI problems appearing in hemodynamics.

We treat the nonlinearities in an explicit way in order to focus on coupling iterations. We compare the two schemes by studying their sensitivity to some physical and discretization parameters. Out of the numerous parameters involved in FPSI problems, only a few have a meaningful impact on the performances of the partitioned procedures. For instance, in the previous subsection we remarked that variations of the hydraulic conductivity produce minor changes in the number of iterations, unlike variations of the porosity.

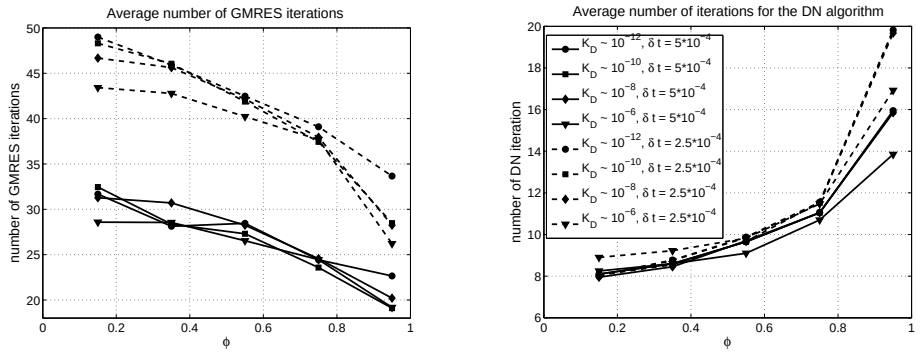

(a) ILUT-GMRES method

(b) DN algorithm

Figure 7: (a) Average number of GMRES iterations to solve the monolithic system and (b) average number of iterations for the DN algorithm for different values of ϕ, κ, and δt. The legend in (b) is common to the two figures.

For all the simulations, we took $\rho_d = 1$ g/cm^3 and $\kappa \sim 10^{-12}$ (cm^3 s)/g, and we used the same mesh of Section 8.3. Figures 8(a), 8(b), and 8(c) show the sensitivity to the time step, porosity, and Young's modulus, respectively. For the results in Fig. 8(a) and Fig. 8(c), we choose the physiological values $\rho_s = 1.1$ g/cm^3, $\phi = 0.15$, while for those in Fig. 8(b) $\rho_s = 100$ g/cm^3. The reason of this non-physiological value is that, if ρ_d and ρ_s are of the same order of magnitude, varying ϕ does not change the criticality of the added-mass effect. In fact, the effect of porosity on the convergence properties of partitioned procedures is simply related to the reduction of the effective structure density. In Fig. 8, we report the results of the RN scheme (with α_f prescribed by (70)), without relaxation and with an Aitken relaxation procedure, and those of the DN algorithm with Aitken acceleration parameters.

We let the time step take four different values, $\delta t = 10^{-3}$, $5{\cdot}10^{-4}$, $2.5{\cdot}10^{-4}$, $1.25{\cdot}10^{-4}$ s and report the results in Fig. 8(a), whereas for those in Fig. 8(b) and 8(c) we set $\delta t = 5 \cdot 10^{-4}$. The porosity in Fig. 8(b) takes all the values used for Fig. 7. Finally, the results reported in Fig. 8(c) we refer to the Young's modulus in Table 1 times a factor β, with $\beta = 1/5$, $1/2.5$, 1, 2.5, 5.

Figures 8 confirm that the RN scheme converges always without relaxation. Furthermore, it is quite insensitive to parameters variations. The insensitivity is even more evident when an Aitken acceleration technique is employed. On the other side, the convergence of the DN algorithm deteriorates as the time step decreases and the porosity increases.

Concluding, the RN algorithm proves to be faster and more robust than the DN scheme also when dealing with FPSI problems.

Figures 8 display only the results of the DN algorithm with an Aitken relaxation method because the algorithm with a constant acceleration parameter becomes dramatically slow for small time step values and large added-mass effects.

Remark 8.1 *The DN scheme adopted for the results presented in this subsection is not a Dirichlet-Neumann algorithm strictly speaking (see Remark 7.1). In order to impose a Dirichlet interface condition on both components of the fluid velocity at the* $(k+1)$*-th*

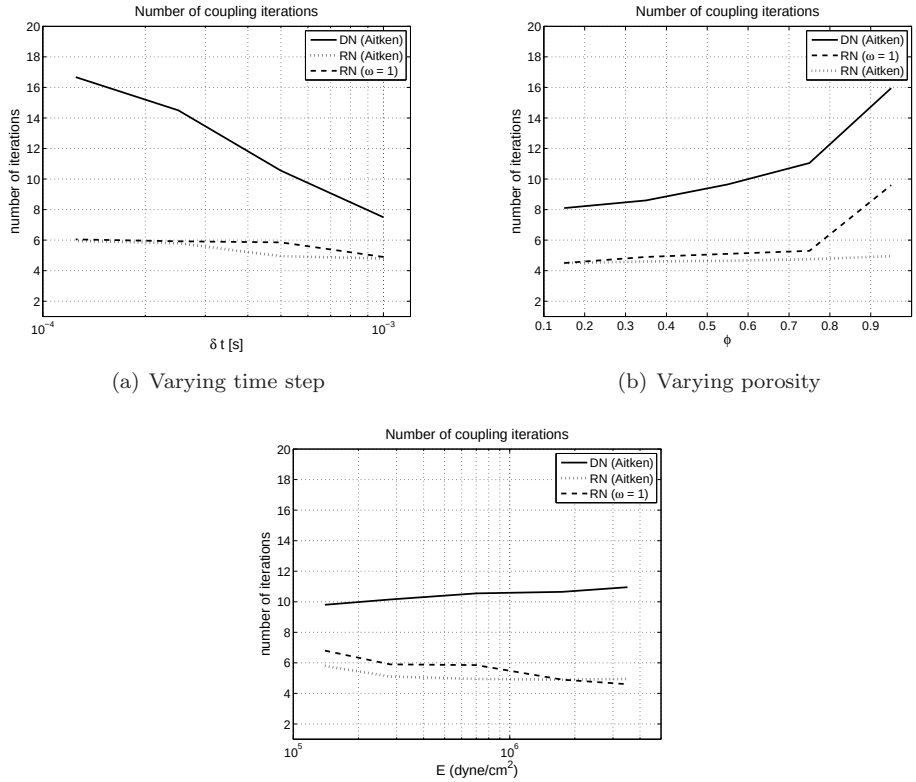

(a) Varying time step

(b) Varying porosity

(c) Varying Young's modulus

Figure 8: Average number of coupling iterations for the DN and RN schemes varying (a) time step δt, (b) porosity ϕ, and (c) Young's modulus E.

iteration, we could replace condition

$$\boldsymbol{u}_f^{k+1} \cdot \boldsymbol{t} + \frac{\sqrt{\kappa}}{\gamma} \boldsymbol{t} \cdot (\boldsymbol{\sigma}_f^{k+1} \cdot \boldsymbol{n}) = \boldsymbol{u}_s^k \cdot \boldsymbol{t},$$

by

$$\boldsymbol{u}_f^{k+1} \cdot \boldsymbol{t} = \boldsymbol{u}_s^k \cdot \boldsymbol{t} - \frac{\sqrt{\kappa}}{\gamma} \boldsymbol{t} \cdot (\boldsymbol{\sigma}_f^k \cdot \boldsymbol{n}),$$

where we omitted the reference to the time level t^{n+1}. We tested also this "proper" DN method but its performance is even worse than that of the "improper" DN scheme. Thus, we disregarded it.

8.5. The RR algorithm

We aim at checking the convergence properties of the RR algorithm with an explicit treatment of the nonlinearities.

In [5], it is pointed out that the estimate of α_s given by (66) does not allow a better performance with respect to the DN method. The reason is that fluid model problem (50) is far too simplified. Hence, instead of choosing the combination factor α_s as in (66), we take $\overline{\alpha}_s = \beta \alpha_s$. Figure 9 shows the number of average coupling iterations for factor

β spanning from 10^{-4} to 1. The results refer to the FPSI problem in hemodynamics: $\rho_s = 1.1$ g/cm^3, $\rho_d = 1$ g/cm^3, $\phi = 0.15$, $\kappa \sim 10^{-12}$ (cm^3 s)/g. The mesh is the same used for the simulations in Section 8.3 and the time step is taken equal to $\delta t = 5 \cdot 10^{-4}$. From Fig. 9, we see that for no factor β the RR algorithm outperforms the RN one. A better estimate for α_s should be studied in order to make the RR method more competitive.

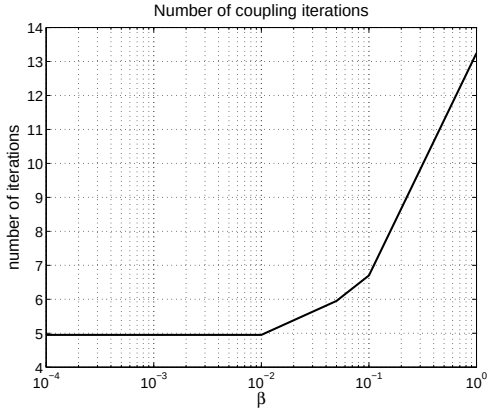

Figure 9: Number of iterations for the RR scheme for different values of factor β.

8.6. Qualitative results

Solving FPSI problems in hemodynamics could help understand how LDL deposit, leading to the formation of atheriosclerotic plaques. Atherosclerosis localizes at a bend and/or bifurcation of an artery, where the LDL can accumulate. Therefore, we consider a $2d$ model obtained by intersecting a bended, stenotic artery with a plane. The geometry we consider (see Fig. 10) is idealized. However, it serves the purpose of showing qualitatively how important it is to account for wall deformation as well as filtration flow.

We impose the same boundary conditions as for the straight artery in [57]. We solve both the Navier-Stokes/transient Darcy and the Navier-Stokes/Biot coupled problems. The former accounts for filtration flow only, neglecting the compliance of the artery wall, whereas the latter models both. The fluid and structure meshes consist of 596 $\mathbb{P}_1$ fluid nodes and 1698 structure nodes, respectively. As for the straight artery, the structure mesh nodes at the interface correspond to the $\mathbb{P}_1 iso \mathbb{P}_2$ degrees of freedom for the fluid velocity. The parameters are those typical of hemodynamics, i.e. the ones listed in Table 1 plus $\rho_d = 1$ g/cm^3, $\kappa \sim 10^{-12}$ (cm^3 s)/g, and $\phi = 0.15$. In the two cases, we adopted a monolithic approach and an explicit treatment of the nonlinearities.

Figure 10 shows the fluid pressure p_f and the pressure of the porous structure p_p every 4 ms in case the structure is governed by the transient Darcy system. Being the fluid incompressible and the structure rigid, the pressure pulse imposed at the inlet does not propagate. Both pressures return to zero when the pulse is over, i.e. after 5 ms. The blood and structure dynamics change completely when the porous medium is deformable, see Fig. 11. The pressure pulse enters the lumen and the poroelastic structure and propagates from the upstream section to the downstream one. Supposing that blood flow and wall movement dictate the transport of the LDL, it is clear that a diffusion-advection model will give significantly different LDL distributions if it uses the solution of the Navier-Stokes/transient Darcy or the Navier-Stokes/Biot system.

9. Conclusions

In this paper we described a new methodology for modeling the fluid-structure problems in hemodynamics. The novelty consists in employing a poroelastic model for the artery wall. The necessary mathematical theory was developed in order to couple a linear poroelastic solid with the nonlinear Navier-Stokes fluid model. We have developed new stabilization techniques for both the transient Darcy problem and Biot system by using a VMS approach. The stabilized system allows to use simple FE spaces for all the unknowns of the problem. We have also introduced the form of the coupled algebraic system that is obtained.

Modular and non-modular solution techniques used for fluid-elastic structure interaction problems have been extended to these more complex interactions. The non-modular approach is based on the ILUT preconditioner for the whole FPSI system. The modular algorithms make use of classical domain decomposition preconditioners: the Dirichlet-Neumann, the Robin-Robin, and the Robin-Neumann ones. Robin conditions are linear combinations of Dirichlet and Neumann conditions. Effective combinations coefficients for the Robin interface conditions have been suggested thanks to simplified fluid and structure models. The convergence properties of the partitioned procedures were analyzed through simplified blood-vessel systems. Also in the case of FPSI problems, the Robin-Neumann algorithm converges always without relaxation and it is fairly insensitive to the added-mass effect, unlike the Dirichlet-Neumann scheme. In the case of a poroelastic structure, the added-mass effect is dictated by the porosity: the bigger the porosity value is, the smaller the effective structure density becomes.

Since there was an interest in the fluid-structure coupling, we dealt with the semi-implicit versions of all the methods mentioned above. This allowed us to focus on the effects of physical and discretization parameters variations on the "stiffness" of the coupling.

Numerical experiments on a straight $2d$ artery agree with the theoretical results found for the partitioned procedures. The monolithic approach confirmed its efficiency in presence of critical added-mass effects. Moreover, we used an idealized bended, stenotic $2d$ artery to show how important it is to adopt the poroelastic model for the simulation of complex problems, such the LDL transport and accumulation in the artery wall.

References

[1] S. Badia and R. Codina. On some fluid-structure iterative algorithms using pressure segregation methods. Application to aeroelasticity. *Internat. J. Numer. Methods Engrg.*, 72:46–71, 2007.

[2] S. Badia and R. Codina. On a multiscale approach to the transient Stokes problem. Dynamic subscales and anisotropic space-time discretization. *Applied Mathematics and Computation*, doi:10.1016/j.amc.2008.10.059, 2008.

[3] S. Badia and R. Codina. Stabilized continuous and discontinuous Galerkin techniques for darcy flow. *UPCommons*, `http://hdl.handle.net/2117/2447`, Submitted.

[4] S. Badia and R. Codina. Unified stabilized finite element formulations for the Stokes and the Darcy problems. *UPCommons*, `http://hdl.handle.net/2117/2168`, Submitted.

[5] S. Badia, F. Nobile, and C. Vergara. Fluid-structure partitioned procedures based on Robin transmission conditions. *J. Comp. Phys*, 227(7027–7051), 2008.

[6] S. Badia, F. Nobile, and C. Vergara. Robin-Robin preconditioned Krylov methods for fluid-structure interaction. Technical Report 19/2008, MOX, Politecnico di Milano, 2008.

[7] S. Badia, A. Quaini, and A. Quarteroni. Modular vs. non-modular preconditioners for fluid-structure systems with large added-mass effect. *Comput. Methods Appl. Mech. Engrg.*, 197(49-50):4216–4232, 2008.

[8] S. Badia, A. Quaini, and A. Quarteroni. Splitting methods based on algebraic factorization for fluid-structure interaction. *SIAM J. Sci. Comput.*, 30(4):1778–1805, 2008.

[9] G. S. Beavers and D. D. Joseph. Boundary conditions at a naturally permeable wall. *J. Fluid Mech.*, 30:197–207, 1967.

[10] M. A. Biot. General theory of three-dimensional consolidation. *J. Appl. Phys.*, 12:155–164, 1941.
[11] M. A. Biot. Theory of elasticity and consolidation for a porous anisotropic solid. *J. Appl. Phys.*, 25:182–185, 1955.
[12] M. A. Biot. Theory of finite deformations of porous solids. *Indiana Univ. Math. J.*, 21:597–620, 1971/72.
[13] P. Bochev, M. Gunzburger, and R. Lehoucq. On stabilized finite element methods for the Stokes problem in the small time-step limit. *Internat. J. Numer. Methods Fluids*, 53:573–597, 2007.
[14] F. Brezzi, J. Douglas, R. Duran, and M. Fortin. Mixed finite elements for second order elliptic problems in three variables. *Numer. Math.*, 51:237–250, 1987.
[15] F. Brezzi, J. Douglas, M. Fortin, and L. D. Marini. Efficient rectangluar mixed finite elements in two and three spaces variables. *Math. Model. Numer. Anal.*, 21:581–604, 1987.
[16] F. Brezzi, J. Douglas, and L. D. Marini. Two families of mixed finite elements for second order elliptic problems. *Numer. Meth.*, 47:217–235, 1985.
[17] F. Brezzi and M. Fortin. *Mixed and hybrid finite element methods*. Springer Verlag, 1991.
[18] F. Brezzi, T.J.R. Hughes, and E. Süli. Variational approximation of flux in conforming finite element methods for elliptic partial differential equations: a model problem. *Rend. Mat. Acc. Lincei s. 9*, 12:167–183, 2001.
[19] V. M. Calo, N. F. Brasher, Y. Bazilevs, and T. J. R. Hughes. Multiphysics model for blood flow and drug transport with application to patient-specific coronary artery flow. *Comput. Mech.*, 43(1):161–177, 2008.
[20] P. Causin, J.F. Gerbeau, and F. Nobile. Added-mass effect in the design of partitioned algorithms for fluid-structure problems. *Comput. Methods Appl. Mech. Engrg.*, 194(42-44):4506–4527, 2005.
[21] B. Chan, P.S. Donzelli, and R.L. Spilker. A mixed-penalty biphasic finite element formulation incorporating viscous fluids and material interfaces. *Annals of Biomedical Enginnering*, 28(589–597), 2000.
[22] M. Chiumenti, Q. Valverde, C. Agelet de Saracibar, and M. Cervera. A stabilized formulation for incompressible elasticity using linear displacement and pressure interpolations. *Comput. Methods Appl. Mech. Engrg.*, 191:5253–5264, 2002.
[23] R. Codina. A discontinuity-capturing crosswind-dissipation for the finite element solution of the convection-diffusion equation. *Comput. Methods Appl. Mech. Engrg.*, 110:325–342, 1993.
[24] R. Codina. Comparison of some finite element methods for solving the diffusion-convection-reaction equation. *Comput. Methods Appl. Mech. Engrg.*, 156:185–210, 1998.
[25] R. Codina. Stabilization of incompressibility and convection through orthogonal sub-scales in finite element methods. *Comput. Methods Appl. Mech. Engrg.*, 190:1579–1599, 2000.
[26] R. Codina. A stabilized finite element method for generalized stationary incompressible flows. *Comput. Methods Appl. Mech. Engrg.*, 190:2681–2706, 2001.
[27] R. Codina. Stabilized finite element approximation of transient incompressible flows using orthogonal subscales. *Comput. Methods Appl. Mech. Engrg.*, 191:4295–4321, 2002.
[28] R. Codina, J. Principe, O. Guasch, and S. Badia. Time dependent subscales in the stabilized finite element approximation of incompressible flow problems. *Comput. Methods Appl. Mech. Engrg.*, 196:2413–2430, 2007.
[29] O. Coussy. *Mechanics of Porous Continua*. John Wiley & Sons, 1995.
[30] S. Deparis. *Numerical analysis of axisymmetric flows and methods for fluid-structure interaction arising in blood flow simulation*. PhD thesis, École Polytechnique Fédérale de Lausanne, 2004.
[31] S. Deparis, M. Discacciati, G. Fourestey, and A. Quarteroni. Fluid-structure algorithms based on Steklov-Poincaré operators. *Comput. Methods Appl. Mech. Engrg.*, 195(41-43):5797–5812, 2006.
[32] M. Discacciati. *Domain decomposition methods for the coupling of surface and groundwater flows*. PhD thesis, École Polytechnique Fédérale de Lausanne, 2004.
[33] M. Discacciati, A. Quarteroni, and A. Valli. Robin–Robin domain decomposition methods for the Stokes–Darcy coupling. *SIAM J. Numer. Anal.*, 45(3):1246–1268, 2007.
[34] H. I. Ene and E. Sánchez-Palencia. Équations et phénomènes de surface pour l'écoulement dans un modèle de millieu poreux. *J. Mécanique*, 14:73–108, 1975.
[35] M.S. Engelman, R.L. Sani, and P. Gresho. The implementation of normal and/or tangential boundary conditions in finite element codes for incompressible fluid flow. *Internat. J. Numer. Methods Fluids*, 2:225–238, 1982.
[36] M.A. Fernández, J.F. Gerbeau, and C. Grandmont. A projection semi-implicit scheme for the coupling of an elastic structure with an incompressible fluid. *Internat. J. Numer. Methods Engrg.*, 69(4):794–821, 2007.
[37] M.A. Fernández and M. Moubachir. A Newton method using exact Jacobians for solving fluid-structure coupling. *Comput. & Structures*, 83(2-3):127–142, 2005.
[38] M. Ferrari. Cancer nanotechnology: opportunities and challanges. *Nature Reviews Cancer*, 3(5):161–171, 2005.
[39] D. K. Gartling, C. E. Hickox, and R. C. Givler. Simulation of coupled viscous and porous flow problems. *Comp. Fluid Dynamics*, 7:23–48, 1996.
[40] T.J.R. Hughes. Multiscale phenomena: Green's function, the Dirichlet-to-Neumann formulation,

subgrid scale models, bubbles and the origins of stabilized formulations. *Comput. Methods Appl. Mech. Engrg.*, 127:387–401, 1995.
[41] T.J.R. Hughes, G.R. Feijóo, L. Mazzei, and J.B. Quincy. The variational multiscale method–a paradigm for computational mechanics. *Comput. Methods Appl. Mech. Engrg.*, 166:3–24, 1998.
[42] T.J.R. Hughes, L. Mazzei, and K.E. Jansen. Large eddy simulation and the variational multiscale method. *Computing and Visualization in Science*, 3:47–59, 2000.
[43] W. Jäger and A. Mikelić. On the boundary conditions at the contact interface between a porous medium and a free fluid. *Ann. Scuola Norm. Sup. Pisa Cl. Sci.*, 23(3):403–465, 1996.
[44] W. Jäger and A. Mikelić. On the interface boundary condition Beavers, Joseph, and Saffman. *SIAM J. Appl. Math.*, 60(4):1111–1127, 2000.
[45] I. P. Jones. Low Reynolds number flow past a porous spherical shell. *Proc. Camb. Phil. Soc.*, 73:231–238, 1973.
[46] N. Koshiba, J. Ando, X. Chen, and T. Hisada. Multiphysics simulation of blood flow and LDL transport in a porohyperelastic arterial wall model. *J. of Biomech. Eng.*, 129:374–385, 2007.
[47] W. J. Layton, F. Schieweck, and I. Yotov. Coupling fluid flow with porous media flow. *SIAM J. Numer. Anal.*, 40(6):2195–2218, 2002.
[48] T. Levy and E. Sánchez-Palencia. On boundary conditions for fluid flow in porous media. *Int. J. Engng. Sci.*, 13:923–940, 1975.
[49] A. Masud and T. J. R. Hughes. A stabilized mixed finite element method for Darcy flow. *Comput. Methods Appl. Mech. Engrg.*, 191:4341–4370, 2002.
[50] A. Masud and T.J.R. Hughes. A space-time Galerkin/least-squares finite element formulation of the Navier-Stokes equations for moving domain problems. *Comput. Methods Appl. Mech. Engrg.*, 146:91–126, 1997.
[51] G. McKay. The Beavers and Joseph condition for velocity slip at the surface of a porous medium. In B. Straugham, R. Greve, and H. Ehrentraut, editors, *Continuum mechanics and applications in geophysics and the environment*, pages 126–139. Springer, Berlin, 2001.
[52] C. Michler, E. H. van Brummelen, and R. de Borst. An interface Newton-Krylov solver for fluid-structure interaction. *Internat. J. Numer. Methods Fluids*, 47(10-11):1189–1195, 2005.
[53] D. P. Mok, W. A. Wall, and E. Ramm. Accelerated iterative substructuring schemes for instationary fluid-structure interaction, in *Computational Fluid and Solid Mechanics*, K.J. Bathe (Ed.), pages 1325–1328. Elsevier, 2001.
[54] M. A. Murad, J. N. Guerreiro, and A. F. D. Loula. Micromechanical computational modeling of reservoir compaction and surface subsidence. *Math. Contemp.*, 19:41–69, 2000.
[55] M. A. Murad, J. N. Guerreiro, and A. F. D. Loula. Micromechanical computational modeling of secondary consolidation and hereditary creep in soils. *Comput. Methods Appl. Mech. Engrg.*, 190(15-17):1985–2016, 2001.
[56] D. A. Nield and A. Bejan. *Convection in porous media*. Springer-Verlag, New York, 1999.
[57] F. Nobile. *Numerical Approximation of Fluid-Structure Interaction problems with application to Haemodynamics*. PhD thesis, École Polytechnique Fédérale de Lausanne, 2001.
[58] A. A. Oberai and P. M. Pinsky. A multiscale finite element method for the Helmohltz equation. *Comput. Methods Appl. Mech. Engrg.*, 154:281–297, 1998.
[59] M. Prosi, P. Zunino, K. Perktold, and A. Quarteroni. Mathematical and numerical models for transfer of low-density lipoproteins through the arterial wall: a new methodology for the model set up with applications to the study of disturbed lumenal flow. *J. Biomechanics*, 38:903–917, 2005.
[60] A. Quarteroni and A. Valli. *Domain Decomposition Methods for Partial Differential Equations*. Oxford Science Publications, 1999.
[61] P. A. Raviart and J. M. Thomas. *A mixed-finite element method for second order elliptic problems*, volume Mathematical aspects of the finite element method, Lecture Notes in Methematics. Springer, New York, 1977.
[62] Y. Saad. *Iterative methods for sparse linear systems*. PWS Publishing, Boston, MA, 1996.
[63] A. G. Saffman. On the boundary condition at the surface of a porous medium. *Studies in Appl. Math.*, 1:93–101, 1971.
[64] A. G. Salinger, R. Aris, and J. J. Derby. Finite element formulations for large-scale, coupled flows in adjacent porous and open fluid domains. *Internat. J. Numer. Methods Fluids*, 18:1185–1209, 1994.
[65] V.A. Salomoni and B. A. Schrefler. Stabilized-coupled modelling of creep phenomena for saturated porous media. *Internat. J. Numer. Methods Engrg.*, 66:1587–1617, 2006.
[66] E. Sánchez-Palencia. *Nonhomogeneous media and vibration theory*. Lecture Notes in Physics. Springer-Verlag, Berlin, 1980.
[67] R. E. Showalter. Poroelastic filtration coupled to Stokes flow. In O. Imanuvilov, G. Leugering, R. Triggiani, and B. Zhang, editors, *Lecture Notes in Pure and Applied Mathematics, vol. 242*, pages 229–241. Chapman & Hall, Boca Raton, 2005.
[68] P. Le Tallec and J. Mouro. Fluid structure interaction with large structural displacements. *Comput. Methods Appl. Mech. Engrg.*, 190:3039–3067, 2001.

[69] J. M. Thomas. *Sur l'analyse numérique des méthodes d'éléments finis hybrides et mixtes*. PhD thesis, Université Pierre et Marie Curie, 1977.

[70] M. Whale, A. Grodzisky, and A. Johnson. The effect of aging and pressure on the patient hydraulic conductivity of the aortic wall. *Biorheology*, 33:17–44, 1996.

[71] P. Zunino. *Mathematical and numerical modeling of mass transfer in the vascular system*. PhD thesis, École Polytechnique Fédérale de Lausanne, 2002.

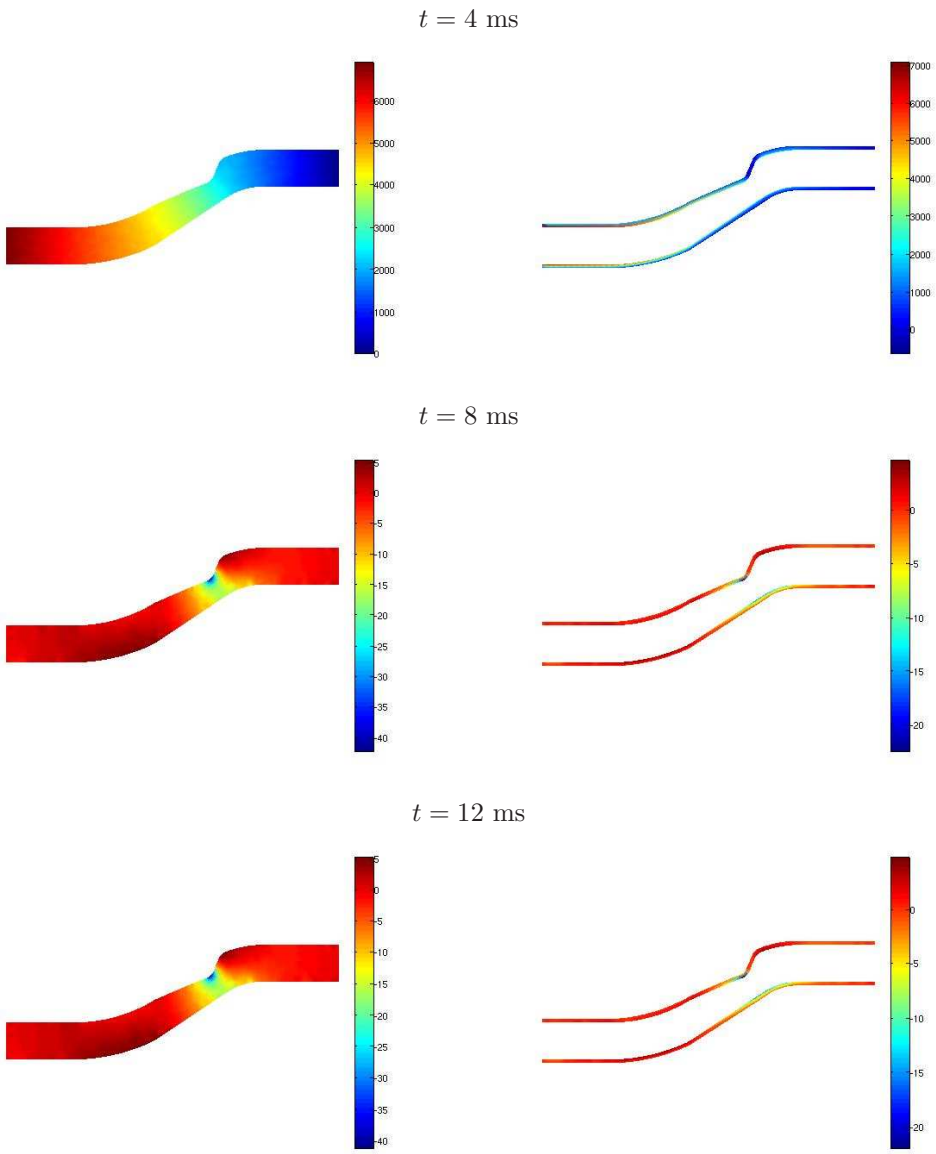

Figure 10: Pressure solution every 4 ms in the fluid and in the rigid porous structure.

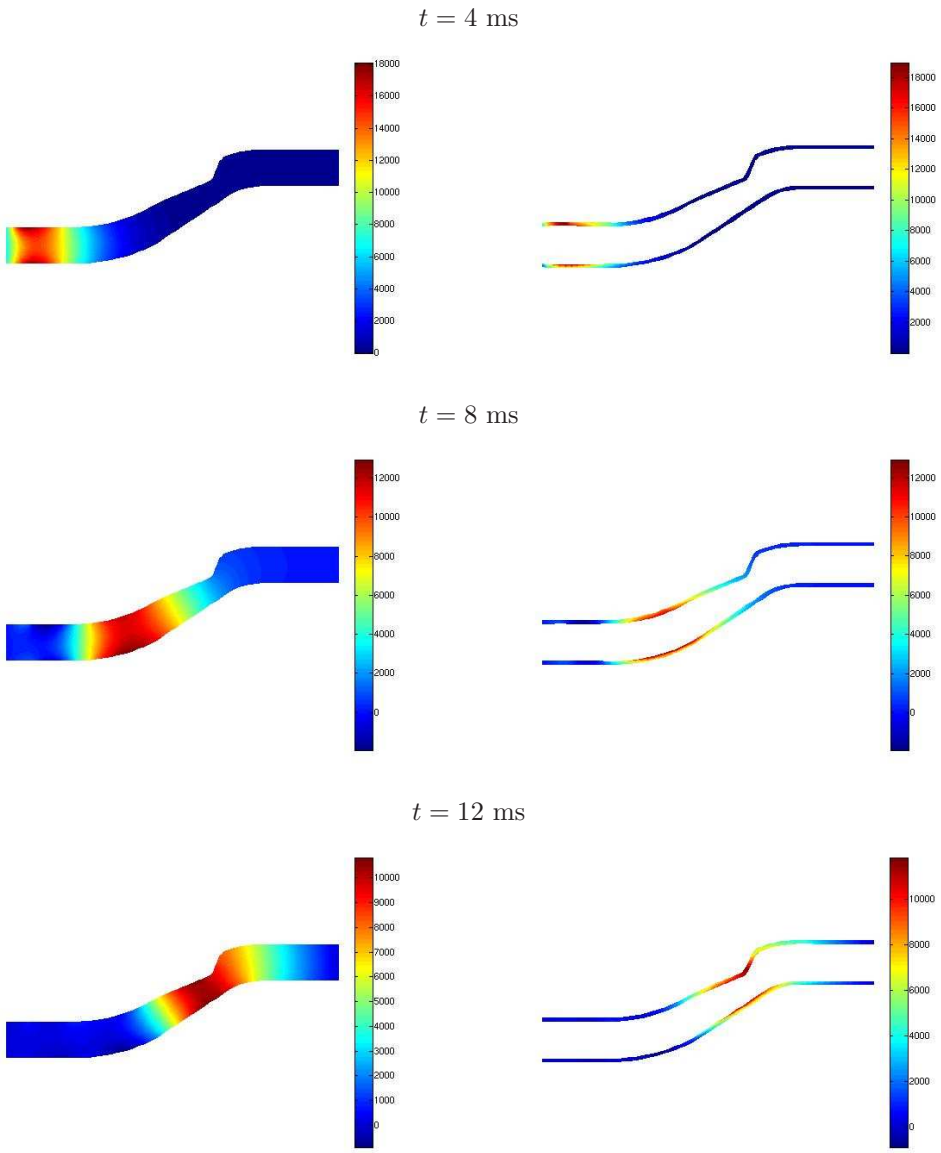

Figure 11: Propagation of the initial pressure pulse in the fluid and in the poroelastic structure. Solution at every 4 ms.